

Gut bacteria-derived succinate induces enteric nervous system regeneration

Begüm Aydın^{1*}, Izabela Mamede^{1,6}, Joana Cardoso^{1,6}, Julia Deere¹, Yelina Alvarez¹, Shanshan Qiao², Ved P. Sharma³, Marissa A. Scavuzzo⁴, Gregory P. Donaldson¹, Chun-Jun Guo², Daniel Mucida^{1,5*}

¹Laboratory of Mucosal Immunology, The Rockefeller University, New York, USA

² Jill Roberts Institute for Research in Inflammatory Bowel Disease, Weill Cornell Medicine, Cornell University, New York, USA

³ Bio-Imaging Resource Center, The Rockefeller University, New York, USA

⁴ Department of Genetics and Genome Sciences, Case Western Reserve University School of Medicine, Ohio, USA

⁵ Howard Hughes Medical Institute, The Rockefeller University, New York, USA

⁶ These authors contributed equally.

*Correspondence: baydin@rockefeller.edu (B.A.) or mucida@rockefeller.edu (D.M.).

Abstract

Enteric neurons control gut physiology by regulating peristalsis, nutrient absorption, and secretion¹. Disruptions in microbial communities caused by antibiotics or enteric infections result in the loss of enteric neurons and long-term motility disorders²⁻⁵. However, the signals and underlying mechanisms of this microbiota–neuron communication are unknown. We studied the effects of microbiota on the recovery of the enteric nervous system after microbial dysbiosis caused by antibiotics. We found that both enteric neurons and glia are lost after antibiotic exposure, but recover when the pre-treatment microbiota is restored. Using murine gnotobiotic models and fecal metabolomics, we identified neurogenic bacterial species and their derived metabolite succinate as sufficient to rescue enteric neurons and glia. Unbiased single-nuclei RNA-seq analysis uncovered a novel neural precursor-like population marked by the expression of the neuronal gene *Nav2*. Genetic fate-mapping showed that *Plp1*⁺ enteric glia differentiate into neurons following antibiotic exposure. In contrast, *Nav2*⁺ neurons expand upon succinate treatment and indicate an alternative mode of neuronal regeneration under recovery conditions. Our findings highlight specific microbial species, metabolites, and the underlying cellular mechanisms involved in neuronal regeneration, with potential therapeutic implications for peripheral neuropathies.

Main

The gastrointestinal (GI) tract is the largest barrier surface through which the body interacts with the external environment. This extensive interface hosts a vast array of immune cells, gut microbiota, enteric nervous system (ENS), and a complex network of neurons and glial cells responsible for regulating essential gastrointestinal functions and responding to diverse environmental signals^{1,6}. The intricate crosstalk between the ENS, gut immune system, and microbiota forms a dynamic microenvironment characterized by a state of chronic yet physiological inflammation. However, the signals and mechanisms that mediate this multifaceted communication remain poorly understood. Disruptions in this balance, often involving alterations in microbial communities, have been implicated in the pathogenesis of post-infectious neuropathies and neurodegenerative and neurodevelopmental disorders^{7,8}. Most enteric neurons and glia are derived from neural crest progenitors that invade the gut during embryogenesis⁹. These progenitors undergo a finely tuned process of self-renewal and differentiation, giving rise to diverse neuronal and glial cell types along the length of the gut¹⁰. Although most ENS cells are generated during embryonic development, a secondary wave of neurogenesis occurs postnatally, coinciding with gut colonization by microbiota¹¹. The microbiota also regulates the postnatal migration of enteric glial cells along the serosa-lumen axis¹². In addition, mice raised under germ-free (GF) conditions have a reduced number of enteric neurons in regions where the density and diversity of microbiota are highest³. This temporal and spatial association suggests a possible role for microbial signals in influencing ENS development and maintenance upon microbial insults. While enteric neurogenesis is thought to cease by weaning under physiological conditions, studies have demonstrated the remarkable plasticity of enteric glial cells, which can differentiate into neurons *in vitro* and *in vivo* following chemical injury or colitis^{11,13-15}. Nonetheless, the molecular signals, particularly those derived from the microbiota, that govern ENS plasticity and the role of microbiota in ENS maintenance and regeneration remain largely unexplored. Here, we investigated the effects of microbiota on the ENS following microbial dysbiosis and colonization in GF mice to uncover the bacterial signals and cellular mechanisms that maintain postnatal plasticity in the ENS.

Microbial manipulations mediate loss and recovery of the enteric nervous system

We have previously shown that microbial dysbiosis induced by antibiotics (Abx) treatment or *Salmonella* *AspiB* infection results in loss of enteric neurons mediated by caspase-11/NLRP6-dependent non-canonical inflammasome pathway^{2,3,16}. Following acute treatment with a single antibiotic ampicillin in wild-type C57Bl/6 mice, we observed loss of both enteric neurons and glia in the distal small intestine (**Fig. 1a, b**). While we observed a decrease in overall Sox10+ glia (**Fig. 1a**), we only included intra-ganglionic glial cells in our quantifications to avoid the contribution of extra-ganglionic glia, whose numbers can fluctuate depending on the imaged tissue thickness. These observations suggest that the ENS displays injury-associated cell loss after antibiotic treatment. To test whether both neurons and glia recover upon microbiota restoration, we designed fecal microbiota transfer experiments from conventional specific pathogen-free (SPF) mice (**Fig. 1c, f, h**). Mice were treated with ampicillin by oral gavage for five days, and age-matched mice from the same genotype were used as fecal donors to minimize microbiota-related differences in all fecal transfer experiments. Ampicillin treatment resulted in dysbiosis with decreased diversity and expansion of *Bacteroides*, as measured by 16S RNA sequencing of the fecal samples. (**Extended Data Fig. 1a**). Both neuron and glia numbers were recovered seven days after fecal transfer in both in-house and Jackson mice with levels similar to their steady-state baseline, depicted as grey-shaded area on individual graphs (**Fig. 1d, g**). The recovery in neuronal numbers also correlated with the recovery in bacterial diversity of steady-state (SPF) animals (**Extended Data Fig. 1a**). In addition, SPF microbiota transfer rescued the transit time defects observed in Abx-treated mice (**Fig. 1e**). However, dysbiotic FMT taken from mice at the time of treatment did not rescue the neuronal and glial numbers, unlike SPF FMT (**Fig. 1g**), corroborating the restoration of dysbiosis driving the observed recovery.

We observed that the total length of the small intestine changes upon antibiotic treatment and recovers to the steady-state length upon fecal transfer (**Extended Fig. 1b**). This raises the question of whether an increase in the total length of the small intestine drives the decrease in neuronal density. To rule out this possibility, we counted the number of neurons and glia per ganglia across all conditions. The average number of neurons, or glia, per ganglia decreased upon Abx treatment, and it recovered upon SPF, but not dysbiotic, FMT (**Extended Fig. 1c**), suggesting that the change

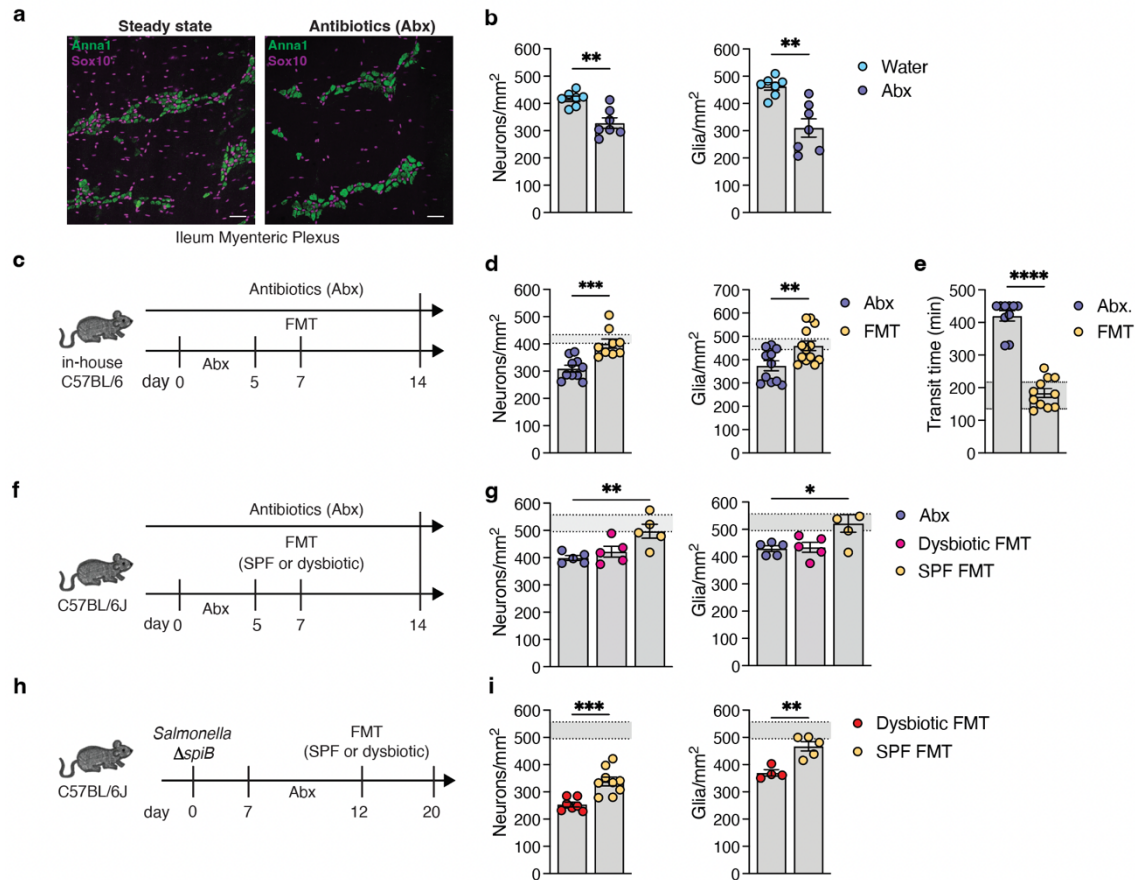


Fig. 1: Microbial-dependent maintenance of enteric neurons and glia. (a) Confocal microscopy images of the ileum myenteric plexus of mice at steady state (left) and five days post-treatment (right) immunostained for ANNA1 and SOX10. Scale bars, 50 μm . (b) Quantification of neurons (Anna1) and intraganglionic glia (Sox10) from mice treated with water or antibiotics for five days ($n=7$). (c) Schematic representation of fecal microbiota transfer (FMT) experiments with in-house C57BL/6 SPF mice after antibiotic treatment. (d) Quantification of neurons (Anna1) and intraganglionic glia (Sox10) from mice treated with antibiotics throughout the experiment (Abx) or that received fecal microbiota transfer (FMT) from SPF mice after antibiotic treatment. Mice were analyzed seven days after FMT ($n=11$ Abx, $n=13$ FMT). The gray shaded line indicates the range of cell numbers at steady state in in-house C57BL/6 mice. (e) Intestinal transit time measurement of SPF mice treated with Abx or that received FMT ($n=10$ Abx, $n=11$ FMT). Mice were analyzed seven days after FMT. The gray shaded line indicates the baseline transit time at the steady state ($n=10$). Data are from two independent experiments. (f) Schematic representation of fecal transfer experiments with dysbiotic and SPF feces from Jackson C57BL/6J mice after antibiotic treatment. (g) Quantification of neurons and intraganglionic glia from C57BL/6J mice treated with Abx alone or those that received FMT from dysbiotic or SPF mice ($n=5$). Mice were analyzed seven days after FMT. (h) Schematic representation of fecal transfer experiments with dysbiotic and SPF feces in Jackson C57BL/6J mice after *Salmonella spiB* infection. (i) Quantification of neurons and intraganglionic glia from C57BL/6J mice treated with Abx only or that received FMT from dysbiotic or SPF mice (neurons, $n=7$ dysbiotic, $n=9$ SPF; Glia $n=4$ dysbiotic, $n=5$ SPF). The gray shaded line indicates the range of cell numbers at steady state in C57BL/6J mice in panels g and i. All data are presented as mean \pm SEM. An unpaired two-tailed Student's t-test was used for panels b, d, e, and i. A one-way ANOVA with multiple hypothesis testing was used for panel g. All data were obtained from the ileum myenteric plexus. Data are from at least two independent experiments, except for glial quantification in panel i.

in neuronal density is not due to changes in the small intestine length. To further rule out that the decrease we observed in neuronal numbers upon Abx treatment was not due to structural changes such as tissue stretching, we measured the average cell-to-cell distance between cell bodies within the ganglia. We did not observe any differences across the conditions (**Extended Data Fig. 1d**). We also did not observe a significant change in either cell number or small intestine length in germ-free mice treated with Abx, suggesting that the effects of Abx are not due to its potential cellular toxicity (**Extended Data Fig. 1e**). Additionally, both neuron and glia loss were absent in 129S1/SvImJ mice, which are deficient in *caspase 11*¹⁷, suggesting that glia loss is also dependent on the non-canonical inflammasome pathway we previously described for enteric neuron loss^{2,3} (**Extended Data Fig. 1f**).

Lastly, we tested whether reversing the dysbiosis induced by *Salmonella AspiB* infection, which causes permanent loss of neurons for up to three months after pathogen clearance², would also rescue neuronal and glial numbers (**Fig. 1h**). Dysbiotic FMT from mice during *Salmonella* infection did not rescue *Salmonella*-induced neuronal and glial loss, whereas SPF FMT rescued both neurons (partially) and glial cells (**Fig. 1i**). These results indicate that enteric neuron and glia loss caused by microbial dysbiosis is reversible upon signals from healthy microbiota.

Microbial-derived succinate induces ENS regeneration

Germ-free mice have fewer enteric neurons in the ileum³, thus providing an experimental platform to identify microbial species and signals sufficient to induce ENS regeneration upon microbiota colonization. We first asked whether colonization of germ-free mice with defined microbial consortia can increase neuronal numbers, as observed upon colonization with fecal microbiota from SPF mice^{3,18}. We tested whether colonization with defined microbial consortia with 12 species (Oligo-MM12) that mimic mouse microbiota¹⁹ would increase the number of neurons in the ileum of germ-free mice. Although we observed a modest increase in the number of neurons upon MM12 colonization, a supplemented version of this consortium with three facultative anaerobes¹⁹ (MM12+3) induced a robust increase in the number of neurons (**Fig. 2a**). We reasoned that one of these facultative anaerobes could be mediating the impact on the observed increase in neuronal numbers. To test whether monocolonization with a single bacterial species, including one of the

facultative anaerobes in MM12+3, was sufficient to increase the number of neurons and glia, we isolated several individual bacterial strains from the MM12+3 consortium and in-house SPF mice. Of those that we tested, the *Escherichia coli* Mt1B1 (*E. coli* Mt1B1) strain was the most potent in increasing both neuronal and glial numbers upon monocolonization in germ-free mice (**Fig. 2b**). Monocolonization with *E. coli* Mt1B1 also increased the number of neurons and glia in outbred Swiss Webster mice, suggesting that the observed neurogenic effect is robust and not confined to an inbred genetic background. (**Extended Data Fig. 2a**).

To identify the molecular signals mediating ENS regeneration, we focused on *E. coli* Mt1B1 and *Bacteroides vulgatus* (*B. vulgatus*) bacterial strains as reductionist models of “neurogenic” and “non-neurogenic” commensal bacteria, respectively. *Bacteroides* and *Escherichia* species differ in the immunogenicity of their lipopolysaccharide (LPS), as *E. coli* has immunostimulatory LPS compared to *B. vulgatus*²⁰. We tested whether the structural difference between the two commensals is sufficient to increase enteric neuron and glial numbers by treating germ-free mice with immunogenic LPS isolated from *E. coli*. We gavaged germ-free mice with *E. coli* LPS and observed no differences in the number of neurons and glia (**Extended Data Fig. 2b**). This prompted us to investigate the signals secreted by the two commensals upon colonization as mediators of ENS regeneration. We performed untargeted liquid chromatography-mass spectrometry (LC-MS) analysis of polar metabolites of cecal contents isolated from mice monocolonized with *E. coli* Mt1B1 and *B. vulgatus* (**Supplementary Data Table 1**). The metabolomic profile of mice monocolonized with *B. vulgatus* was similar to that of GF mice, while mice monocolonized with *E. coli* Mt1B1 differed in the PC1 component in the principal component analysis (PCA), mirroring the ENS quantification phenotype (**Extended Fig 2c**). We also included cecal contents from mice treated with Abx to narrow down the target metabolites expected to be downregulated in the neuronal loss state (**Fig. 2c**). We focused on metabolites that were enriched in mice monocolonized with *E. coli* but downregulated in *B. vulgatus* and Abx-treated mice as potential signals mediating neuronal regeneration. Among these candidates, short- and medium-chain fatty acids, such as propionic acid and succinate, were enriched upon *E. coli* monocolonization, which are the end products of bacterial fermentation (**Fig. 2c**).

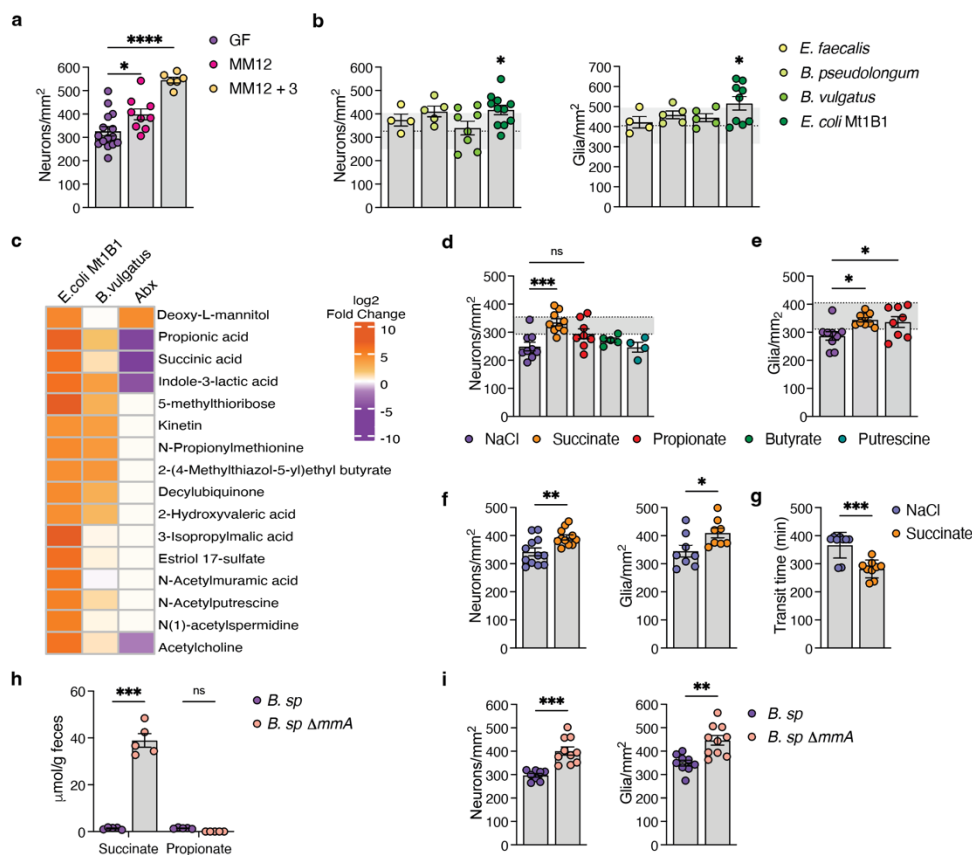


Fig. 2: The bacteria-derived metabolite succinate is sufficient to induce ENS regeneration. (a) Quantification of neurons per mm² of germ-free (GF) and mice colonized with defined communities (n= 15 GF, n=9 MM12, n=6 MM12+3). (b) Quantification of neurons (left) or intraganglionic glia (right) per mm² of mice monocolonized with individual bacterial species. GF numbers are labeled in the range, and the dashed line indicates the average neuronal or glial numbers in GF mice from a. n=4 *E. faecalis*, n= 5 *B. pseudolongum*, n=8 (neurons) and n=5 (glia) for *B. vulgatus*, n=11 (neurons) and n=9 (glia) *E. coli* Mt1B1. (c) Selected metabolite heatmap of cecal content from mice monocolonized with *E. coli* Mt1B1, *B. vulgatus*, and SPF mice treated with Abx for five days (n=5). (d) Quantification of neurons per mm² in Swiss Webster GF mice treated with metabolites in drinking water for seven days (n=9 NaCl, n=9 succinate, n=8 propionate, n=5 butyrate and putrescine). (e) Quantification of intraganglionic glia per mm² of Swiss Webster GF mice treated with metabolites in drinking water for seven days (n=9 NaCl, n=9 succinate, n=8 propionate). The shaded line indicates the recovered range in Swiss *E. coli* monocolonization in d, e. (f) Quantification of neurons (left) and intraganglionic glia (right) per mm² area previously Abx-treated mice that received NaCl or Succinate in drinking water for seven days (neurons, n= 12 NaCl, n=11 succinate. Glia, n=8). (g) Intestinal transit time of mice that received NaCl or Succinate in drinking water for seven days after Abx treatment (n= 9). Data are from at least two independent experiments. (h) HPLC-MS quantification of Succinate and Propionate levels in GF mice monocolonized with *B. sp.* or *B. sp. Δmma* for 7-10 days (n=5) (i) Quantification of neurons (left) and intraganglionic glia (right) per mm² area in GF mice monocolonized with *B. sp.* or *B. sp. Δmma* for seven days (n=10). Data are from two independent experiments. All data are mean ±S.E.M. An unpaired two-tailed Student's t-test was used for f, g, h, i. One-way ANOVA with multiple hypothesis testing was used for b, d, and e. A two-way ANOVA with multiple hypothesis testing was used for h. All data are from the ileum myenteric plexus. Data are from at least two independent experiments except for the metabolomics in c and Butyrate and Putrescine groups in d.

Short-chain fatty acids (SCFAs) are known to influence a wide range of host physiological processes, such as differentiation of immune cells, regulation of gut motility, neuronal activity, and the neurochemical code of enteric neurons^{18,21–24}. We also observed an increase in polyamine-related metabolites, such as N-acetylputrescine and N-acetylspermidine, which we previously showed to be neuroprotective against enteric infection-induced neuronal loss². To test whether these metabolites can increase the number of neurons, we treated germ-free mice with metabolites in drinking water *ad libitum*. Succinate treatment increased both neuron and glial numbers in germ-free mice (**Fig. 2d**), while propionate had a modest gliogenic effect (**Fig. 2e**). We noted that succinate levels were also increased in the FMT state as opposed to Abx (**Extended Data Fig. 2d**). To test whether increased succinate levels could also rescue Abx-induced neuronal and glial loss, we administered succinate to SPF mice previously treated with Abx. Both neuron and glial numbers were recovered upon succinate treatment following Abx, further validating the robustness of its neurogenic and gliogenic properties (**Fig. 2f**). Succinate also rescued the increased transit time defect in Abx-treated mice (**Fig. 2g**). Finally, we orthogonally validated the effect of succinate by monocolonizing germ-free mice with the commensal protist *Tritrichomonas musculus* (*T. musculus*), which has been shown to excrete high levels of succinate upon colonization in germ-free mice²⁵. Consistent with succinate administration in drinking water, colonization with *T. musculus* also increased enteric neurons and glia in germ-free mice (**Extended Data Fig. 2e**).

Succinate is an intermediate metabolite in the fermentation of dietary fibers into SCFAs by gut commensals and provides critical energy substrates for host and microbial cells²⁶. Additionally, succinate regulates the gut-immune axis by inducing type 2 immunity, regulating intestinal cell proliferation, and influencing the metabolic control of cell fate specification^{26–30}. As a gain-of-function strategy for “non-neurogenic” *Bacteroides* species, we used a genetically engineered version of the *Bacteroides* species with a mutation in its carbohydrate catabolic pathway (*B. sp. 1_1_6 Δmma*)³¹. When CO₂ levels are limited, *Bacteroides* species can regenerate CO₂ via methylmalonyl-CoA mutase enzyme that isomerizes succinate into methylmalonate, which is then decarboxylated to generate CO₂ and propionate^{32,33} (**Extended Data Fig. 2f**). The *Bacteroides* species 1_1_6 Δmma (*B. sp. Δmma*) that is mutant in its methylmalonyl-CoA mutase enzyme cannot metabolize succinate; therefore, it excretes high levels of succinate in the lumen upon

monocolonization in germ-free mice as measured by targeted LC-MS profiling (**Fig. 2h**). High levels of succinate in the gut lumen were sufficient to robustly increase both the number of neurons and glia upon monocolonization^{27,28} (**Fig. 2i**). We conclude that intestinal bacteria-derived succinate induces regeneration in adult murine ENS.

Identification of ENS precursors associated with ENS recovery

The ENS develops from vagal and sacral neural crest-derived progenitors that migrate along the developing gut, giving rise to neurons and glia with a highly coordinated self-renewal and differentiation pattern⁹. Although postnatal neurogenesis in the ENS ceases around weaning age, our observations above suggest that specific mechanisms are in place to replenish dying neurons following GI insults. However, little is known about the mechanisms mediating peripheral neuronal recovery. One possibility raised in previous studies is glia-to-neuron differentiation in chemical injury or colitis models^{14,34}. Another possibility is the continuous turnover of adult ENS from Nestin-expressing progenitor cells³⁵. We first sought to identify the origin of neuronal recovery observed upon FMT to understand how neurons regenerate in adult stages. We optimized single-nuclei RNA sequencing (snRNA-seq) in the mouse gut for unbiased characterization of ENS cell populations across different microbiota conditions. We isolated nuclei from the *ileum muscularis* layer of mice in steady state, Abx, and three days post-FMT conditions to cover the early steps in neuronal commitment. After density-gradient purification of isolated nuclei from ileum muscularis layers, we sequenced ~20,000 nuclei per condition using the 10X genomics platform.

UMAP clustering of individual libraries showed distinct separation of mesenchyme-like and ENS clusters (glia, neuron, progenitor/immature neuron-like) annotated by gene set enrichment analysis using the EnrichR algorithm depicted as the top 10 pathways enriched per cluster³⁶ (**Extended Data Fig. 3a-d**). To test whether the proportion of progenitor/immature neuron-like clusters changes across conditions, we focused on the clusters with neuron, glia, and immature neuron or progenitor-like identity within individual conditions, integrated them across conditions, and re-clustered them using UMAP clustering within the Seurat R toolkit³⁷. Cells with neuronal expression signatures were separated into five clusters, and those with glial signatures

were divided into two clusters based on marker gene expression for specific cell types (**Fig. 3a-c**). We did not observe significant changes between the frequency of these clusters across conditions, except for cluster 4, which was enriched in the Abx condition; thus, we labeled it as the stress/injury cluster (**Fig. 3b**). We observed the enrichment of a small cluster with a neuronal signature and cycling genes, which we labeled progenitor/immature neuron-like cells (cluster 9). Cluster 9 (c9) was enriched in the Abx and FMT states and was characterized by the expression of cycling genes such as *Top2a* and *Mki67* (**Fig. 3b, c**). Gene set enrichment analysis showed that synaptogenesis and neurotransmitter release-related pathways were enriched in glial and neuronal clusters. In contrast, pathways associated with programmed cell death were enriched in the stress/injury cluster specific to the Abx state (cluster 4), and pathways related to neuronal development were enriched in the precursor-like c9 (**Fig. 3d**). We searched for differentially enriched genes in the stress/injury and precursor-like clusters using the Seurat FindMarkers function. Among the differentially expressed genes, the stress/injury cluster differentially expressed *Gsdme* and *Mcu*, both of which are implicated in mitochondrial damage leading to neuronal death^{34,35} (**Fig. 3e**). The precursor-like cluster was enriched in cell cycle-related genes such as *Top2a*, chromatin regulator *Ezh2*, and the retinoic acid-responsive gene *Nav2*, which is shown to be involved in neuronal migration and neurogenesis in the central nervous system (CNS)³⁸ (**Fig. 3f**). To assess the potential of precursor-like cell populations to give rise to neurons and glia, we used the Wishbone algorithm, which orders cells based on their developmental progression and pinpoints bifurcation points in cell-fate acquisition³⁹. We used the precursor-like cluster along with glial clusters as input into the algorithm owing to their co-expression of neuronal and glial genes (**Fig. 3c**). The Wishbone algorithm suggested a path starting from the precursor-like cluster and bifurcating into glial and neuronal branches, with the most differentiated cells labeled in red (**Fig. 3g, h**). Gene expression changes along the trajectory showed the expression of *Nav2* and glial-marker *Plp1* in the precursor-like cluster at the beginning of the trajectory (**Fig. 3i**). As the trajectory progressed, glial markers (*Sox5* and *Plp1*) became restricted to the glial branch. In contrast, the neuronal marker *Elavl4* was restricted to the neuronal branch. Collectively, these results show the enrichment of a precursor-like cluster marked by *Nav2* expression and suggest that cells in this cluster have the potential to give rise to neurons and glia.

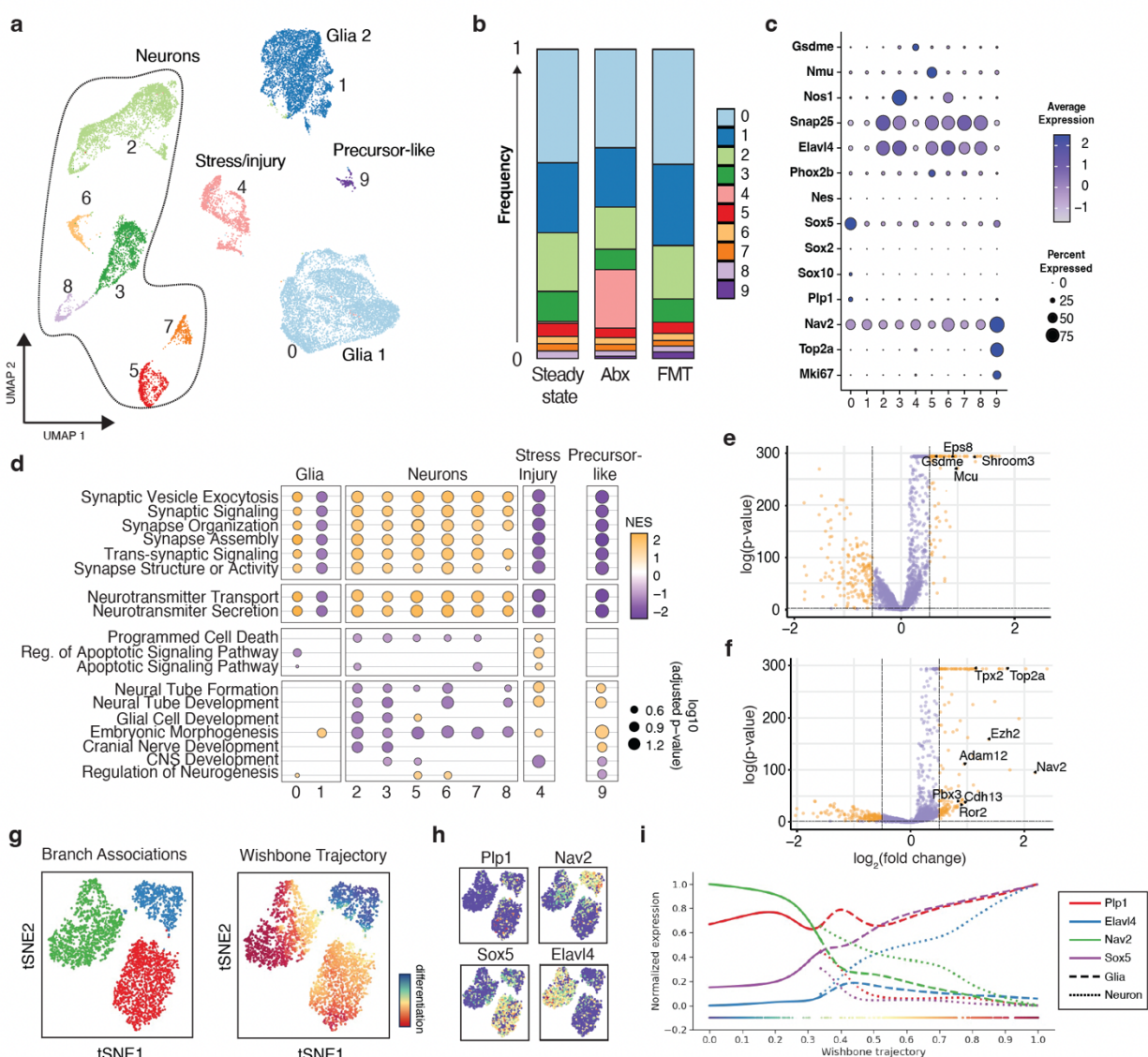


Fig. 3: Single-nuclei RNA-seq (snRNA-seq) profiling of myenteric plexus cell populations reveals a precursor-like cluster enriched in the FMT state. (a) UMAP clustering of subsetted and merged datasets of nuclei isolated from the muscularis layer of steady state, Abx, and FMT mice analyzed three days post-FMT (n=4, pooled). (b) Bar plot displaying the frequency of each cluster under individual conditions. (c) Dot plot of representative marker gene expression in separate clusters. (d) Gene set enrichment analysis (GSEA) of annotated clusters. (e) Volcano plot of genes differentially expressed in the injury/stress cluster (c4) compared to the rest of the clusters. (f) Volcano plot of genes differentially expressed in the precursor-like cluster (c9) compared to the rest of the clusters. (g) tSNE plot showing the branch association identity (left) and Wishbone trajectory (right) with the gradient of cell differentiation scores. (h) tSNE plot showing the expression of glial (*Plp1* and *Sox5*), neuronal (*Elavl4*), and precursor-like cluster (*Nav2*) genes along the Wishbone trajectory. (i) Normalized expression levels of glial, neuronal, and precursor-like genes along the Wishbone trajectory.

Plp1+ glia differentiate into neurons during the injury state

Currently, there are no genetic tools available to specifically target Nav2+ cells to test whether the precursor-like population is the source of the observed neuronal regeneration. Nevertheless, the expression of the enteric glial marker Plp1 in the precursor-like population (c9) prompted us to directly test whether Plp1+ glial cells can give rise to neurons upon microbial signals, as previously described during chemical injury and colitis^{14,34}. We designed complementary glial fate-mapping strategies. First, we crossed the Tamoxifen-inducible Plp1^{creERT} mouse strain with the *INTACT* nuclear reporter line that expresses super-folding GFP fused to a nuclear membrane protein in the Rosa26 locus⁴⁰. We administered tamoxifen (Tx) on the last day of Abx treatment and traced whether the labeled Plp1+ cells acquired neuronal identity upon FMT by immunohistochemistry coupled with confocal imaging (**Fig. 4a, b**). We observed approximately 10% Plp1+ neurons in the absence of Tx, indicating the leakiness of the inducible driver (**Fig. 4c**). The 10% misexpression rate in neurons was similar to that of the Tx-only control, suggesting little or no glia-to-neuron differentiation or turnover at steady state (**Fig. 4c**), which is consistent with previous studies suggesting limited neurogenesis in the adult ENS under steady-state conditions^{13,15}. The percentage of fate-mapped neurons significantly increased to approximately 25% upon Abx treatment, as well as upon Abx treatment followed by FMT; no significant differences were observed between the Abx and FMT groups (**Fig. 4c**). This suggests that glia-to-neuron differentiation is initiated during the “stress/injury” state, even though only FMT can rescue neuronal or glial cell numbers. To gain insights into the cellular mechanism of observed neuronal recovery, we tested if Plp1+ cells divide before they give rise to neurons with the thymidine analog, 5-Ethynyl-2'-deoxyuridine (EdU), labeling dividing cells. The percentage of EdU+ Plp1 cells was low (0.4%) and did not differ between the Abx and FMT conditions as measured by flow cytometry (**Extended Data Fig. 4a**). These results suggest that direct enteric glia-to-neuron conversion may limit neuronal loss post-injury, although this process is unlikely to be solely responsible for the complete ENS recovery induced by FMT.

Growing evidence suggests enteric glial cell heterogeneity at the molecular, chromatin, and functional levels^{41,42}. To complement Plp1-based fate-mapping and test whether other subtypes of enteric glia could also give rise to neurons, we used Tx-inducible Sox10^{creERT2} and GFAP^{creERT2}

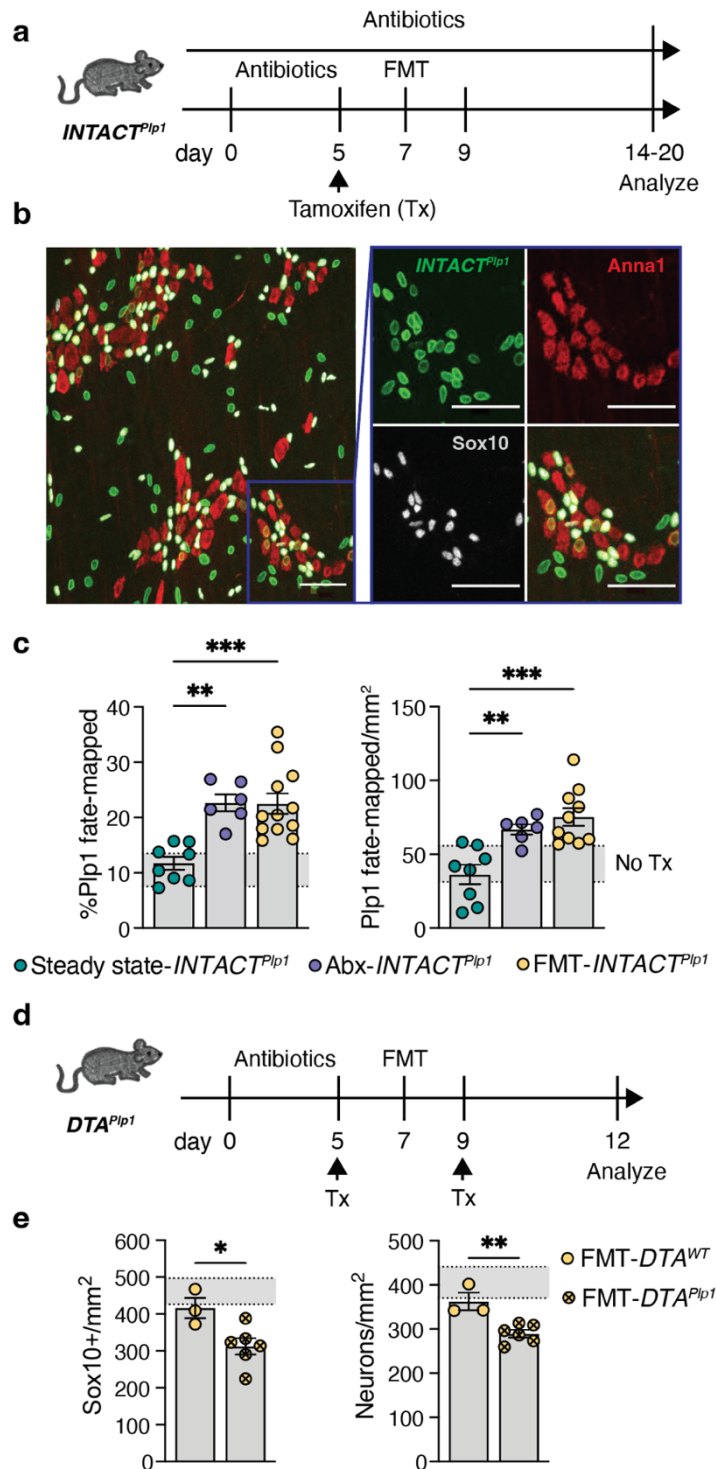


Figure 4: Plp1+ glia differentiate into neurons during the Abx state. (a) Schematic representation of the experimental design of the Plp1 glial fate-mapping experiment. (b) Confocal microscopy images of the ileum myenteric plexus of *INTACT^{Plp1}* (green) reporter mice immunostained for ANNA1 and Sox10. The inset shows a zoomed-in version of the area designated by the square. Scale bars, 50 μm . (c) Quantification of the percentage of *INTACT^{Plp1}+Anna1+* cells over total Anna1+ cells (left) and the number of *INTACT^{Plp1}+Anna1+* cells per mm^2 of ileum myenteric plexus 7-10 days post-Abx or FMT ($n=8$ steady state, $n=6$ Abx, $n=12$ FMT). Steady-state mice were only treated with tamoxifen and harvested a day or three weeks later. The shaded grey line indicates the baseline in No Tamoxifen controls. Data are representative of at least two experiments. (d) Schematic representation of the experimental design of *DTA^{Plp1}* glia ablation experiment. (e) Quantification of intraganglionic Sox10+ glia (left) and Anna1+ (right) neurons per mm^2 in *DTA^{WT}* ($n=3$) and *DTA^{Plp1}* ($n=5$) mice five days after FMT. The shaded line indicates the range of neuronal numbers in WT mice at steady state. All data are mean \pm S.E.M. A one-way ANOVA with multiple hypothesis testing was used for c. An unpaired two-tailed Student's t-test was used for e.

drivers to fate-map different populations of glia upon microbiota manipulation (**Extended Data Fig. 4b**). We did not observe as much leakiness in Sox10^{creERT2} as we did in the Plp1^{creERT} mice, as the no-Tx control showed approximately 5% expression in neurons (**Extended Data Fig. 4c**). However, 20% of the neurons were Sox10+ cells at steady state within 24 h of tamoxifen induction, likely a result of misexpression of the construct in neurons, rather than steady-state Sox10+ glia-to-neuron differentiation, given the short time frame post labeling (**Extended Data Fig. 4c**). No significant changes in the percentage of Sox10+ fate-mapped neurons were observed between the Abx, FMT, and steady-state groups (**Extended Data Fig. 4c**). This suggests that Sox10+ neurons do not represent a major contributor to the neuronal regeneration observed post-microbial manipulations.

A recent study suggested that GFAP+ glia are restricted to the myenteric ganglia and poised to generate neurons at the chromatin accessibility level in neuronal genes⁴³. Hence, we also tested whether GFAP+ glia can give rise to neurons upon microbial manipulation by crossing GFAP^{creERT2} and *INTACT* nuclear reporter mouse strains. We did not observe GFAP+-labeled cells acquiring neuronal signatures in any condition, suggesting that GFAP+ glia do not contribute to neuronal regeneration upon microbial signals (**Extended Data Fig. 4d**).

To directly address the possible contribution of Plp1+ glial cells in limiting neuronal loss during Abx-mediated injury, we crossed the inducible Plp1^{creERT} driver with Rosa26^{DTA} mice, enabling the expression of diphtheria toxin A upon Tx induction in Plp1-expressing cells. Plp1 is also expressed in CNS oligodendrocytes and Schwann cells that myelinate peripheral neuron axons⁴⁴. Thus, ablation causes off-target effects that restrict the timeline of the analysis. Despite these technical challenges, we administered Tx at the end of antibiotic treatment (**Fig. 4d**) and measured ablation efficiency by immunohistochemical staining for Sox10+ glia. We observed an approximately 10% decrease in Sox10+ glia when Plp1+ cells were ablated during FMT (**Fig. 4e, Extended Data Fig. 4e**). Neuronal numbers did not fully recover upon ablation of Plp1+ cells, providing additional evidence for a contribution from Plp1-glia derived neurons in limiting neuronal loss post-Abx-mediated injury (**Fig. 4e**). Notably, we also observed a decrease in the number of neurons when Plp1+ cells were ablated at a steady state, indicating a physiological role for Plp1+ glia in neuronal

maintenance (**Extended Data Fig. 4f**). We noticed that ablating Plp1+ cells at steady-state and Abx conditions resulted in a higher loss of Sox10+ glia than the FMT condition, suggesting a distinct origin for Sox10+ glial regeneration induced by FMT signals (**Extended Data Fig. 4e**). These results indicate that Plp1+ glia, but not Sox10+ or GFAP+ glial cells, differentiate into neurons upon microbiota manipulation, limiting overall neuronal loss post-injury.

Succinate increases Nav2+ neurons during recovery

The above results indicate that increased Plp1+ glia-to-neuron differentiation occurs in the injury/Abx state, although neuronal numbers do not fully recover without FMT or succinate treatment. It is plausible that signals from microbiota, including succinate, can indirectly reduce tissue inflammation to help maintain the survival of newly born neurons, resulting in a net gain in neuronal numbers. A non-mutually exclusive possibility is that recovery signals can initiate an alternative mode of neuronal regeneration from another source. To distinguish between these possibilities, we first tested whether succinate contributes to Plp1+ glia-to-neuron differentiation using our Plp1-based fate-mapping approach (**Extended Data Fig. 4g**). Instead, we observed a decrease in the percentage of Plp1+ fate-mapped neurons in the succinate group compared to that in the vehicle control group (**Extended Data Fig. 4h**). As the neurons did not fully recover in the control group, the reduction in fate-mapping percentage upon succinate treatment suggests an additional source of neuronal regeneration in the recovery state.

Next, we investigated whether succinate-induced neuronal recovery in the gnotobiotic setting is mediated by Plp1+ glia-to-neuron differentiation. To this end, we re-derived the *Plp1*^{INTACT} line under germ-free conditions to fate-map Plp1+ glia-to-neuron differentiation upon monocolonization with WT vs. succinate-producing mutant *B. sp. AmmA*. We labeled Plp1+ cells with sterile Tx a day before monocolonization with WT *B. sp.* and *B. sp. AmmA* in sealed positive-pressure isocages (**Fig. 5a**). We did not observe any differences in Plp1+ fate-mapped neurons (**Fig. 5b**), reinforcing that Plp1+ glia-to-neuron differentiation does not occur in the absence of stress/injury signals under gnotobiotic conditions.

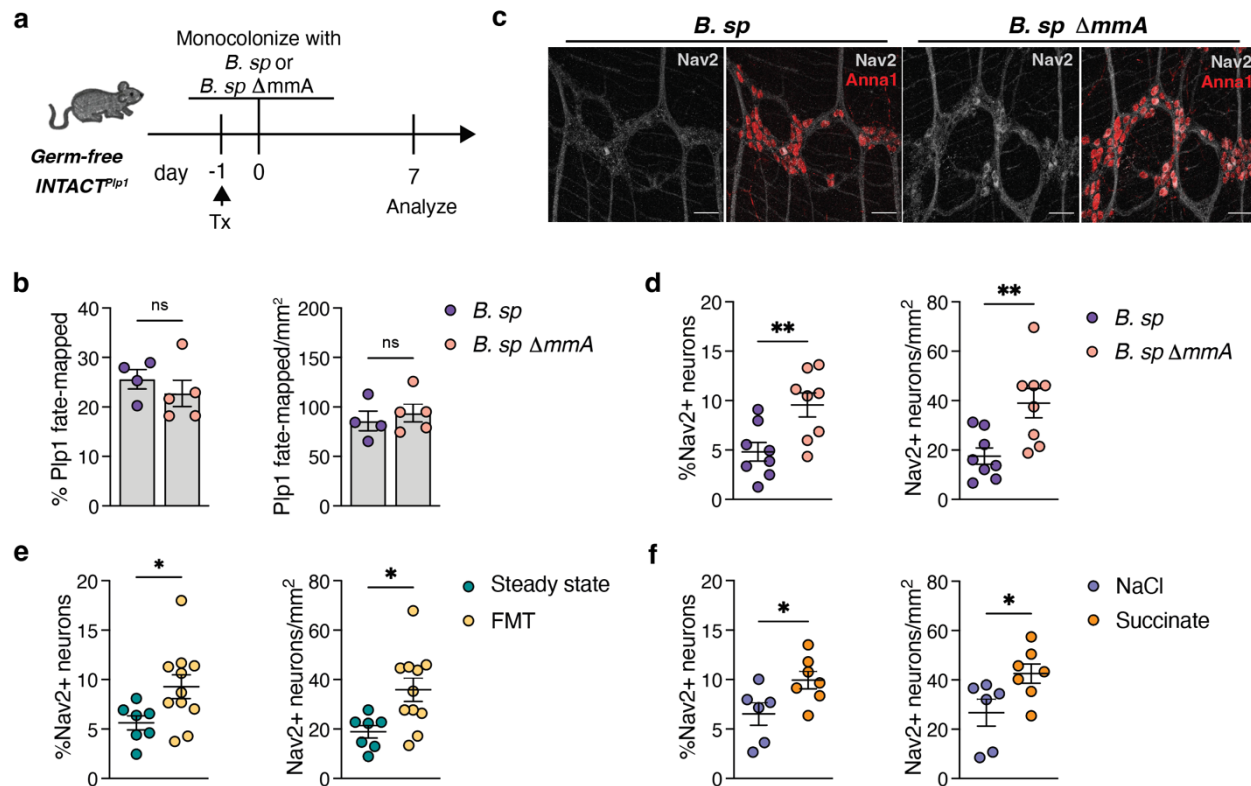


Fig. 5: Expansion of Nav2+ neurons upon succinate treatment. (a) Schematic representation of the experimental design of Plp1 glia fate-mapping experiment in GF mice monocolonized with *B. sp*. or *B. sp. ΔmmaA*. (b) Quantification of percentage of Plp1+Anna1+ cells over total Anna1+ cells (left) and number of Plp1+Anna1+ cells per mm² of ileum myenteric plexus seven days post-monocolonization (n=4 *B. sp*, n=5 *B. sp ΔmmaA*). (c) Confocal microscopy images of ileum myenteric plexus of monocolonized mice immunostained for ANNA1 and Nav2. Scale bars, 50 μm. (d) Quantification of the percentage of Nav2+Anna1+ cells over total Anna1+ cells (left) and number of Nav2+Anna1+ cells per mm² of ileum myenteric plexus seven days post-monocolonization (n=8 for both groups). Data are from at least two independent experiments. (e) Quantification of the percentage of Nav2+Anna1+ cells over total Anna1+ cells (left) and number of Nav2+Anna1+ cells per mm² of ileum myenteric plexus at steady state (n=7) or seven days post-FMT (n=11). Data are from at least two independent experiments. (f) Quantification of the percentage of Nav2+Anna1+ cells over total Anna1+ cells (left) and number of Nav2+Anna1+ cells per mm² of ileum myenteric plexus seven days post-NaCl (n=6) or succinate (n=7) treatment in previously Abx-treated mice. Data are from at least two independent experiments. All data are mean ±S.E.M. An unpaired two-tailed Student's t-test was used for all graphs.

Finally, we investigated whether succinate mediates the *de novo* increase in neuronal numbers by expanding the novel precursor-like population identified in the FMT state by snRNA-seq (cluster 9). We monocolonized germ-free mice with WT *B. sp*. and succinate-producing *B. sp. ΔmmaA* and stained for Nav2, which was differentially expressed in this precursor-like cell cluster. We observed cytoplasmic Nav2 protein expression in enteric neurons within the ganglia (Fig. 5c). The

percentage and total number of Nav2+ neurons significantly increased in *B. sp.* Δ mmA-monocolonized mice, suggesting an alternative pathway independent of Plp1+ glia-to-neuron differentiation (Fig. 5d). Consistently, the percentage of Nav2+ neurons also increased in the FMT and succinate-induced recovery following Abx (Fig. 5e, f). These results suggest that microbiota-derived succinate increases the Nav2+ neural precursor-like population as an alternative pathway for neuronal regeneration.

Discussion

This study identified gut bacterial species with neurogenic vs. non-neurogenic roles, and the bacterial metabolite succinate as a downstream signal sufficient to regenerate enteric neurons and glia in adult mice. Fate-mapping of enteric glial populations enabled us to identify Plp1+ glia-to-neuron differentiation as a neuronal recovery mechanism initiated in the injury or Abx state. Therefore, it is plausible that enteric glia may be involved in tissue surveillance that detects damage and enables rapid regeneration onset upon injury with replacement components at hand⁴⁵. However, the increase in Nav2+ neurons suggests an alternative mechanism through the expansion of a novel precursor-like population identified in our unbiased characterization of the muscularis layer during microbiota-mediated recovery, presumably by the process of maturation or recruitment of precursors. While the ENS regenerates at a steady state from mature glial cells in zebrafish for example⁴⁶, in mammals, neurogenesis or neuronal regeneration does not occur in adults, except in the olfactory bulb and hippocampus^{47,48}. The mechanisms of neuronal regeneration described here could represent an evolutionary adaptation sustaining organismal fitness by regenerating neurons damaged by environmental perturbations, such as toxins, infections, or inflammation^{4,5}.

Growing evidence suggests cellular plasticity of enteric glia in adult stages. Recent studies highlight the neurogenic potential of enteric glial cells by retaining an open chromatin state at critical early ENS progenitor loci^{43,49}. Our results on Plp1+ glia-to-neuron differentiation align with these recent observations and provide functional validation of the plasticity of enteric glial populations that respond to environmental stimuli. However, it is unclear whether cell division occurs during glial-to-neuron differentiation post-injury. One interpretation for the limited EdU labeling in Plp1+

glia is the induction of transdifferentiation of glia into neurons instead of dedifferentiation into a progenitor state⁵⁰. A non-mutually exclusive possibility for the lack of EdU incorporation would be a shortened S phase⁵¹ or cell division without new DNA synthesis involved⁵².

Our results point to bacteria-derived succinate as an important mechanism inducing neuronal recovery. Succinate may mediate neuronal recovery directly by acting on ENS precursors expressing its cognate G-protein coupled receptor *Sucnr1* (*Gpr91*)⁵³, although our snRNA-seq dataset did not capture its expression by the ENS. Succinate may act on immune or non-hematopoietic cells such as Tuft cells^{27,28}, which would then initiate neuronal recovery possibly via expansion or migration of Nav2+ cells. A recent study indicated an anti-inflammatory role for intracellular succinate released upon exercise in skeletal muscle, which results in neurotrophic and muscle extracellular matrix remodeling⁵⁴. Our results reveal bacterial signals and metabolites that induce neuronal regeneration and propose a model by which neuronal maintenance upon microbial insults is achieved in the adult stages. This discovery can be harnessed to develop therapies for post-infectious neuropathies and regenerative medicine.

Author contributions

B.A. conceived, performed, analyzed all experiments, interpreted results, and wrote the manuscript. I.M. analyzed the 16S and snRNA-seq data. J.C. performed and analyzed experiments and contributed to mouse treatments, imaging and quantification, snRNA-seq, and 16S. J.D. performed and analyzed experiments, and contributed to the imaging and quantification of ENS, and intestinal transit time experiments. Y.A. contributed to the mouse treatments, dissections, and metabolomic extractions. S.Q. performed and analyzed the targeted SCFA metabolomics. V.P.S. performed custom image analysis. M.A.S. contributed to the trajectory analysis of the snRNA-seq data. G.P.D. assisted with microbiology. C.G. provided guidance and mutant bacterial strains. D.M. conceived, supervised the study, and co-wrote the manuscript. All authors have read the manuscript.

Acknowledgements

We thank A. Rogoz for germ-free mice maintenance; A. Bilate and A. Rogoz for the germ-free rederivation of the glial reporter line; T. Ahrends and B. Reis for help with flow cytometry. M. Fischbach (Stanford) for insightful suggestions on the metabolomics data; E. Gerrick and M. Horowitz (Stanford) for kindly providing the *T. musculus*; R. Hamnett and J. A. Kaltschmidt (Stanford) for their suggestions on structural analysis of the ganglia; B. Fait and N. Heintz (Rockefeller) for INTACT mice, Ken Cadwell (Penn) for MM12+3 defined consortia mice, J. Faith (Mt. Sinai) for bacterial isolates of *B. vulgatus* and *B. pseudolongum*, M. Koenen for her insights on nuclei sequencing protocol optimization, and H. Alwaseem and M. Isay-Del Viscio for fecal metabolomics instrumentation and analysis at the Rockefeller University Proteomics Resource Center; The Rockefeller University Sequencing Core for their help with sequencing 10X libraries and additional Rockefeller University employees for continuous assistance; and Zeny A. for emotional support. Finally, we gratefully acknowledge the mice used in this study for enabling these discoveries. Metabolomics data were generated by the Proteomics Resource Center at Rockefeller University ([RRID:SCR_017797](https://www.rockefeller.edu/RRID:SCR_017797)) using instrumentation funded by the Sohn Conferences Foundation and the Leona M. and Harry B. Helmsley Charitable Trust. Confocal microscopy was performed at the Rockefeller University's Bio-Imaging Resource Center (RRID:SCR_017791). V.P.S. is supported by the Beckman Foundation award, AWD00000407. This work was supported by a grant from the Simons Foundation (718232, B.A.), H.H.M.I. Hanna H. Gray Fellowship (GT15986, B.A.), NIH R01DK126407 (D.M.), Food Allergy FARE/FASI Consortium (D.M.). D.M. is an investigator of H.H.M.I.

Methods

Mice

Mice were maintained at the Rockefeller University animal facilities under specific pathogen-free or germ-free conditions. In-house C57BL/6 or Jackson Labs C57BL/6J (000664) mice were used as wild-type mice, unless otherwise noted. Plp1^{creERT}(B6.Cg-Tg (Plp1-cre/ERT)3Pop/J, Jackson 005975); 129S1/SvImJ, (Jackson 002448); Sox10^{creERT2} (B6;CBA-Tg(Sox10-cre)1Wdr/J, Jackson 025807); GFAP^{creERT2} B6.Cg-Tg(GFAP-cre/ERT2)505Fmv/J, Jackson 012849); Rosa26^{DTA} (B6.129P2 *Gt(ROSA)26Sor^{tm1(DTA)Lky}*/J, Jackson 009669); Rosa26^{INTACT} (B6.129-*Gt(ROSA)26Sor^{tm5.1(CAG-Sun1/sfGFP)Nat}*/MmbeJ, Jackson 030952) transgenic mice were purchased and

maintained under specific pathogen-free conditions on a standard chow diet in our facility. Genotyping was performed according to the protocols established for the respective strains by The Jackson Laboratories using the Transnetyx genotyping services. C57B6 and Swiss-Webster germ-free mice were purchased from Taconic Biosciences and maintained on a sterilized and autoclaved mouse diet (Cat:5021, LabDiet). The *Plp1^{INTACT}* line was re-derived in a germ-free isolator and maintained on autoclaved food and water *ad libitum*. All mice were used starting at 7-12 weeks of age unless otherwise noted and housed under a 12-hour light/12-hour dark cycle with food and water *ad libitum*. Male or female sex-matched mice were pooled for all experiments because no significant differences between the sexes were observed in any of the analyzed parameters. Because of the limited number of mice interbred in our facility, not all experiments were performed with littermates. We did not control for the estrous cycle. All mice were handled according to protocols approved by the Institutional Animal Care and Use Committee (IACUC) within the ethical guidelines of the National Institutes of Health (NIH) Guide for the Care and Use of Laboratory Animals.

Antibiotics treatment

Five milligrams of ampicillin (Sigma-Aldrich) per mouse was administered via 100 μ L oral gavage for 5–14 days, as indicated in the experiment. An antibiotic cocktail of 6.25 mg/ml of vancomycin (Sigma-Aldrich), 6.25 mg/ml of ampicillin (Sigma-Aldrich), 12.5 mg/ml of metronidazole (Sigma-Aldrich), and 12.5 mg/ml of neomycin (Sigma-Aldrich) (VAMN) was administered to *Salmonella* Δ *spiB*-treated mice for five days via oral gavage (100ul/mouse) before fecal microbiota transfer. Abx administration to germ-free mice was performed in sealed positive pressure isocages with 1 g/L ampicillin in vacuum-sterilized (Corning) drinking water for seven days.

Tamoxifen treatment

Tamoxifen (Sigma-Aldrich) was dissolved in sterile corn oil and ethanol (10%) to a concentration of 50 mg/ml. *Plp1^{creERT}* mice received 7.5 mg/ml tamoxifen by oral gavage for induction. We noticed increased off-target effects in neurons with multiple doses of Tamoxifen for this *Plp1^{creERT}*, thus limiting the fate-mapping experiments to one injection unless otherwise noted. *Sox10^{creERT2}*

mice were gavaged 7.5 mg/ml tamoxifen, and GFAP^{creERT2} mice were gavaged 12.5 mg/ml twice, as indicated in the experiment.

Fecal microbiota transfer

Fresh feces (two pellets) from age-matched (or litter-matched whenever available) SPF mice were dissolved in 1 ml PBS and filtered with a 70 μ M cell strainer. Oral gavage of 200 μ l/mouse fecal mixture was performed, and mice were kept in cleaned cages for the experiment. *Salmonella* Δ *spiB*-*treated* mice received five days of VAMN antibiotic cocktail before fecal microbiota transfer as described above. For dysbiotic FMT transfers, the fecal pellets on the last day of treatment with Abx or *Salmonella* Δ *spiB* were frozen at -20°C, dissolved in PBS, and administered to the same mice, as described above.

Salmonella *spiB* infection

Infections with *Salmonella* Δ *spiB* were performed as previously described². Briefly, mice were pretreated with a single oral dose of streptomycin (20 mg/mouse in 100 ml of DPBS) 18-24 hours before infection. The mice were then orally inoculated with 10⁹ CFU of *Salmonella* *spiB*. A single aliquot of *Salmonella* Δ *spiB* strain was grown overnight in 3 mL of LB at 37°C with agitation. Bacteria were subcultured (1:300) into 3 mL of LB and incubated for 3.5 hours at 37°C with agitation. The pellet was resuspended to the final concentration in 1 mL of DPBS. Bacteria were administered by oral gavage at a total volume of 100 μ L per mouse.

Bacterial cultures and colonization of germ-free mice

Bacteria were cultured in Brain Heart Infusion media (BHI, Becton Dickinson 211059) supplemented with 5 μ g/ml hemin (Sigma 51280) and 1 μ g/ml vitamin K (Sigma 95271). Mouse isolates were cultured either aerobically for *Escherichia coli* (Mt1B1) and *Enterococcus faecalis* (KB1)¹⁹ or in an anaerobic atmosphere of 85% nitrogen, 10% carbon dioxide, and 5% hydrogen for *Bacteroides vulgatus* (RU1) and *Bifidobacterium pseudolongum* (RU3). *Bacteroides* sp. 1_1_6 (*B. sp* WT and Δ mma)³³ strains were grown with 15 μ g/ml thiamphenicol (Fisher Scientific). Germ-free mice were colonized with *Escherichia coli* Mt1B1, *Bacteroides vulgatus*, *Bifidobacterium pseudolongum*, *Bacteroides* sp. 1_1_6 (*B. sp.* Δ mma)³³ bacterial cultures grown to confluency

by oral gavage of 200 μ l/mouse in sealed positive pressure isocages. Mice were sacrificed and harvested after 7-10 days of colonization for enteric nervous system staining and imaging, as indicated per the experiment. Colonization was checked by qPCR with species-specific primers or plating on BBL Brain Heart Infusion (BHI) + agar bacterial plates.

***Tritrichomonas musculus* colonization of germ-free mice**

Frozen vials of *T. musculus* were thawed in a 37°C water bath and resuspended in 3 ml RPMI media without serum. The viability of protists was assessed using a hemocytometer under a bright-field microscope. The cells were centrifuged for 5 min at 100 \times g and resuspended in PBS for the inoculation of mice. Germ-free mice were inoculated with *T. musculus* ~100,000 cells per mouse by oral gavage in sealed isocages²⁵.

LPS treatment

Phenol-purified Lipopolysaccharides (LPS) from *E. coli* O127:B8 (Sigma-Aldrich) were dissolved in autoclaved drinking water and filter-sterilized. Germ-free mice were gavaged daily for five days at a concentration of 5 mg/kg. The mice were harvested two days after treatment.

Administration of bacterial metabolites

The following metabolites were administered to germ-free mice in sealed positive pressure isocages or previously SPF mice treated with antibiotics, as described above, in drinking water: 300 mM Sodium Chloride (Sigma-Aldrich), 150 mM Sodium Succinate (Alfa Aesar)²⁷, 150 mM Sodium Propionate (Sigma-Aldrich), 150 mM Sodium Butyrate (Sigma-Aldrich), and 150 mM putrescine (Sigma-Aldrich). For germ-free mice, the dissolved metabolite solutions were filtered under a sterile hood using 500 ml vacuum filters (Corning).

EdU administration

0.8 mg/ml EdU (Thermo Fisher Scientific) dissolved in drinking water and given to mice ad libitum for 14 days. Fresh EdU water was supplied every two–three days.

Intestinal transit time and length measurements

To measure the total intestinal transit time, mice were administered an oral gavage of 6% carmine red (Sigma-Aldrich) dissolved in 0.5% methylcellulose (prepared with sterile 0.9% NaCl). Transit time was recorded as the duration from oral gavage until the mice passed a fecal pellet containing carmine red. The experiments were concluded after 450 min, designated as the cut-off time for mice that had not passed fecal pellets.

The mice were sacrificed to measure the small intestine length. The small intestine was cut distal to the stomach, carefully pulled out to detach it from the mesenteric tissue, and cut proximal to the ileocecal junction. The length of the whole small intestine was measured by laying it vertically alongside a measuring tape.

Intestine dissections

Mice were sacrificed, the intestine was detached from the mesenteric tissue, and 4-5 cm proximal to the ileocecal junction was taken as the ileum. For dissection of the muscularis, the above segment of the whole tissue was laid flat serosa facing up, and the muscularis layer was carefully peeled off using curved forceps, as described in more detail here⁵⁵.

16S sequencing

Fresh feces were collected for endpoint analysis. Sample preparation for 16S rRNA sequencing was performed by following the 16S Illumina Amplicon protocol from the Earth Microbiome Project⁵⁶. MiSeq 2 × 150 using a 15% PhiX spike was used for the sequencing of the libraries. Sequence processing and downstream analysis were performed in R. In summary, assembly into amplicon sequence variants (ASVs) and taxonomic classification using the Silva database were carried out with Dada2 (v1.2.6). Taxa that were observed fewer than 10 times in at least 20% of the samples were excluded from the analysis. ASV/OTU quantification and related analyses were conducted using Phyloseq(v1.42)⁵⁷ and ggplot2(v3.5.1).

Extraction of cecal content for LS-MS

The feces were flash-frozen in liquid nitrogen. Frozen feces stored at -70°C were freeze-dried. Dried feces were weighed, and 30–40 mg were mixed with 800 µL of 80% methanol, 20% RNase,

and DNase-free water. The samples were vortexed and sonicated for 10 min in a high-power sonicator. Samples were centrifuged at 13 000 rpm at 4°C for 15 min. The supernatant was collected and stored at -70°C until submission for LS-MS.

Untargeted metabolomics of cecal contents

Mouse fecal extracts were analyzed by LC-MS/MS (QExactive Plus orbitrap mass spectrometer coupled to a Vanquish UPLC System, Thermo Fisher Scientific). External mass calibration was performed every three days using a standard calibration mixture. Polar Metabolites were separated by HILIC Chromatography (ZIC-pHILIC 150 x 2.1mm column, EMD Millipore) @150uL/min) using an analytical gradient decreasing from 90% B to 40% B in 30 minutes (A: 20 mM Ammonium Carbonate in Water adjusted to pH 9.3 and B: 100% Acetonitrile). The solvents were of LCMS grade quality (Optima, ThermoFisher). Each sample was analyzed in both positive and negative modes in separate injections. All MS/MS data were collected using Data-Dependent Acquisition (Resolution for Full-Scan:70,000, Resolution for Data-Dependent MS/MS Scans: 17500). Generated data were queried against MZCloud using Compound Discover 3.3 (Thermo Fisher). For matched molecules for which in-house standards were available, retention times were compared to the standards. The peak intensities of the MS/MS data were used to produce plots using Metaboanalyst⁵⁸. The heatmap was plotted in R using the ggplot2 (v3.5.1) and pheatmap (v1.0.12) packages.

Quantification of SCFAs with HPLC-MS

We constructed standard curves of acetate, propionate, and butyrate based on the Area Under Curve (AUC) of true chemical standards at different concentrations to quantify propionate and butyrate. Approximately 20 mg cecal samples were resuspended in 200 µL of 50% MeOH (in H₂O) and vortexed for 10 min (beads (0.1x0.55 mm) were added to disperse the cecal material). Then, the mixture was spun down, and 10 µL of supernatant was mixed with 190 µL short-chain fatty acid (SCFAs) derivatization solution (1 mM 2,2'-dipyridyl disulfide, 1 mM triphenylphosphine, and 1 mM 2-hydrazinoquinoline dissolved in acetonitrile). The resulting mixture was vortexed, incubated at 60 °C for 1 h, and then centrifuged at 21000 × g for 20 min. The supernatant was analyzed using an Agilent 1290 LC system coupled to an Agilent 6530 quadrupole time-of-flight

(QTOF) mass spectrometer with a 130 Å, 1.7 µm, 2.1 mm × 100 mm ACQUITY UPLC BEH C18 column (Waters). We used the following solvent system: A: H₂O with 0.1% formic acid; B: Methanol with 0.1% formic acid. One microliter of each sample was injected, and the flow rate was 0.35 mL/min with a column temperature of 40 °C. The gradient for HPLC-MS analysis was: 0-6.0 min, 99.5%-70.0% A; 6.0-9.0 min, 70.0%-2.0% A; 9.0-9.4 min, 2.0% A; 9.4-9.6 min, 2.0%-99.5% A. Peaks were assigned by comparison with authentic standards and relative analyte concentrations were quantified by comparing their peak areas with those of internal standards. The concentrations of propionate and butyrate were calculated using a standard curve and normalized to cecal weight.

For the detection of succinate, ~ 20 mg cecal samples were resuspended in 200 µL of 50% MeOH (in H₂O) and vortexed for 10 min (some beads (0.1x0.55 mm) were added to disperse the cecal material). Then, the mixture was centrifuged at 21000 × g for 20 min, and the supernatant was analyzed using an Agilent 1290 LC system coupled to an Agilent 6530 quadrupole time-of-flight (QTOF) mass spectrometer with a 1.7 µm, 2.1 × 100 mm ACQUITY UPLC® BEH C18 column (Agilent). The following solvent system was used: A: H₂O with 0.2% formic acid; B: Methanol with 0.1% formic acid. One microliter of each sample was injected, and the flow rate was 0.35 mL/min with a column temperature of 40 °C. The gradient for HPLC-MS analysis was: 0-4.0 min 99.5% A-30.0% A, 4.0-4.5 min 30.0% A-2.0% A, 4.5-5.4 min 2.0% A-2.0% A, 5.4-5.6 min 2.0%A-99.5% A, with the instrument parameters settings as follows: collision and cooling gas, high-purity argon (Ar); nebulizing gas, high-purity nitrogen (N₂, 1.5 L/min); gas temperature, 350 °C; collision energy, 40 kV; mode, negative mode; MS scan range, m/z 100-1600. The concentrations were calculated using a standard curve and normalized to cecal weight.

Immunohistochemistry

Immunohistochemistry analysis of the myenteric plexus was performed as previously described⁵⁵. Briefly, samples were fixed in 4% PFA overnight, washed in 1X PBS, and permeabilized in 0.5% Triton X-100/0.05% Tween-20/4 µg heparin (PTxwH). Samples were then blocked for two hours in blocking buffer (PTxwH with 5% BSA and 5% normal goat serum) at room temperature with gentle agitation. The samples were incubated with primary antibodies in blocking buffer for two days at 4°C with gentle shaking. After primary antibody incubation, the samples were washed four

times in PTxwH and incubated with secondary antibodies for two hours at room temperature. The samples were washed four times in PTwxH and mounted using Fluoromount-G mounting medium (Thermo Fisher Scientific). The following antibodies were used for immunohistochemistry experiments: ANNA-1 (1:200, Gift of Dr. Vanda A. Lennon), Sox10 (1:400 Ab227680), and Nav2 (1:500 Invitrogen PA5-52851). Fluorophore-conjugated secondary antibodies were either H&L or Fab (Thermo Fisher Scientific) at a consistent concentration of 1:400 in the following species and colors: goat anti-rabbit (AF488/568/647) and goat anti-human (AF488/568/647).

Neuronal imaging and neuronal density quantification

Z-stack images of whole-mount samples were acquired on a Zeiss LSM 780 AxioObserver microscope with a Plan-Apochromat 25x/0.8 NA objective lens. A minimum of 8-15 images were randomly captured from a whole-mount muscularis sample. The Fiji cell counter tool was used to count the number of cells in each field⁵⁹. Anna1 images were quantified using Cellpose v3.0.7⁶⁰. We did not observe significant differences between manual and Cellpose counting of Anna1 images. Intraganglionic Sox10+ cells were counted and depicted on the graphs as glia. These counts were then multiplied by a factor of 3.125 (for a 25x objective) to calculate the number of neurons per square millimeter (mm²). The average from eight or more images was then calculated and plotted, with each point on the graph representing an individual mouse. The percentage of fate-mapped or Nav2+ neurons was calculated as divided by the total number of Anna1+ cells per image.

Neurons per ganglia and nearest neighbor cell-to-cell distance quantification

Large-field, tiled, two-channel, Z-stack images were acquired on a Zeiss LSM 780 AxioObserver microscope with a Plan-Apochromat 25x/0.8 NA objective lens. Each image was 1024 × 1024 pixels in XY with a voxel size of 0.55 μm x 0.55 μm x 1.00 μm. For image processing, maximum-intensity Z-projections were generated for each image. czi image in Fiji v2.14.0/1.54k using a custom script. The ganglion boundary was manually marked in each image using the following criteria. A myenteric ganglion was defined as a continuous group of ANNA1+ cells separated by less than 15 μm. Only the complete ganglia were counted per field of view. Therefore, the following ganglia were excluded: 1. Ganglia truncated, 2. No clear separation (> 15 μm) was noted between the last

ANNA1+ cell and the edge of the field of view. Single ANNA1+ cells separated by 15 μm on all sides were counted as extraganglionic. The quantifiable ganglia were averaged for at least 10 images per gut segment per animal. The Z-projection images were imported into QuPath v0.5.1, and all subsequent processing was performed in batch using custom Groovy scripts. Neuronal soma within each ganglion was identified in the ANNA1 channel with Cellpose v3.0.7, and BIOP Cellpose extension v0.9.3, with the following parameters: model=cyto3 and diameter=15 pixels. Partial neurons that touched the ganglion boundary were removed. Delaunay clustering with a centroid-to-centroid distance threshold=45 μm was used to identify the ANNA1+ nuclei cluster in each ganglion. The following measurements from the QuPath project were exported in a CSV file: image name, ganglion annotation name, Delaunay minimum distance, Delaunay number of neighbors, and cluster size. Raw CSV data were analyzed in Excel using pivot tables. ANNA1+ cells with a cluster size < 3 were filtered out. The total number of ANNA1+ cells in each ganglion was calculated and averaged for each mouse. For glia per ganglion quantification, nuclei within each ganglion were identified in the SOX10 channel with Cellpose v3.0.7 and BIOP Cellpose extension v0.9.3, with the following parameters: model=cyto3 and diameter=10 pixels. Partial nuclei touching the ganglion boundary were removed. Delaunay clustering with a centroid-to-centroid distance threshold=35 μm was used to identify the SOX10+ nuclei cluster in each ganglion. SOX10+ nuclei with a cluster size < 3 were filtered out. The total number of SOX10+ cells in each ganglion was calculated and averaged for each mouse. The nearest-neighbor cell-to-cell distance was averaged for each ganglion. All plots and statistical tests were performed using GraphPad Prism v10.2.1.

Nuclei isolation from the muscularis layer

Mice were sacrificed. The small intestine was carefully detached from the mesenteric tissue, and 4-5 cm of the ileum was laid flat on a pre-chilled metal dissection block. The muscularis layer was carefully removed using curved forceps, placed in pre-chilled Eppendorf tubes, and frozen on dry ice. Frozen samples were stored at -80°C for up to a few weeks or processed immediately. To isolate the nuclei, frozen muscularis samples were taken from -80°C and immediately placed into pre-chilled gentleMACS C-tubes (Miltenyi Biotech) and chopped with scissors for 20 seconds in 2 ml Nuclei Extraction Buffer (1M Tris-HCl, 5M NaCl, 1M MgCl_2 , 0.1% Tween with 0.04%BSA). The

samples were placed on a gentleMACS Octo Dissociator (Miltenyi Biotech) and run on the built-in m_muscle program three times. The samples were immediately placed on ice for 10 min, occasionally swirling every 2-3 minutes. The samples were filtered directly on 30 μ M MACS SmartStrainers (Miltenyi Biotech) and centrifuged at 500 \times g for 5 min to isolate the nuclei. The supernatant was washed twice with nucleus-wash buffer (1% BSA in PBS). Additional iodixanol purification was used for the snRNA-seq experiment, as described in the section below.

Nuclei Flow Cytometry

The nuclei of Plp1^{INTACT} mice were isolated as described above. Click-iT Plus EdU Alexa Fluor 647 Flow Cytometry Assay Kit (Thermo Fisher Scientific C10634) was used according to the manual for visualizing EdU+ cells by flow cytometry. DAPI was used to stain the nuclei. The samples were acquired using a BD Biosciences FACSymphony A5 Cell Analyzer. Gating strategies for Plp1^{INTACT} mice muscularis nuclei flow with EdU were as follows: DAPI+GFP+EDU +. Data was analyzed using FlowJo v10.10.

Single-nuclei RNA-seq (snRNA-seq)

The mice were sacrificed, 5 cm of distal ileum muscularis per mouse was carefully peeled off, and the tissue was frozen at -80°C. Four mice were pooled per condition into pre-chilled gentleMACS C tubes and nuclei were extracted as described above by adding Protector RNase Inhibitors (Milipore-Sigma) at a concentration of 0.2U/ μ L to Nuclei Extraction buffer and 1U/ μ L to Nuclei Wash buffer. The following density-gradient purification was done for the extracted nuclei: After washing once with 500 μ L Nuclei Wash Buffer with RNase inhibitors, the pellets were resuspended in Sucrose buffer with RNaseq inhibitors (1M Tris-HCl, 5M NaCl, 1M MgCl₂, 320 nM sucrose, 1U/ μ L Protector RNase inhibitors) and gently mixed with 50% Iodixanol solution. The sample was underlaid with 30% iodixanol solution using an 18 g needle, and again with 35% iodixanol solution (35%, 30%, 25% bottom to top). The samples were centrifuged at 10000g for 20 min at 4°C. The nuclei pellet formed between the 35% and 30% layers was carefully collected with a pipette. The pellet was resuspended in Nucleus Wash Buffer with RNase inhibitors and centrifuged for 5 min at 500 g. The nuclei pellet was gently resuspended in Nuclei Wash Buffer with RNase inhibitors and counted with an INCYTO C-chip hemocytometer (VWR) using a 1:1 ratio of 0.4% Trypan

blue solution. The samples were immediately processed with a 10X Genomics Chromium Next GEM Single Cell 3' kit v3.1, according to the manufacturer's protocol.

Analysis of snRNA-seq data

Bulk tissue snRNA-seq libraries were sequenced on an Illumina NovaSeq S2 flow cell. Alignment to the mouse reference genome mm10 and generation of count matrices were performed on Cell Ranger (v7.0.1) with default parameters and `intron-mode = TRUE`. Abx data outputted 58,788 cells with median genes per cell of 1,544, FMT outputted 39,201 and 1,771 genes per cell, and steady state data outputted 49,156 cells and 1,045 median expressed genes. Filtered feature barcode matrices were then imported to the R environment using Seurat (v4.4.0), and all further analyses were performed in R. Cells with mitochondrial gene expression higher than 10% and a maximum RNA count per cell higher than 9000 were removed to avoid doublets and dying cells. Samples were then individually scaled by SCT transform, and all PCA, UMAP, and clustering possibilities were calculated. After processing, the Abx data had 58,150 cells, FMT 38,586, and steady state 49,043 cells. The final clustering resolution (SCT 0.1) was determined according to the biological differences between cell types. Cell type annotation was performed using the EnrichR method in packages ClusterProfiler⁶¹ (v4.6.2) and fgsea⁶² (v1.24.0) and manual curation. Clusters that had a non-mesenchymal signature were then selected, merged, and re-clustered. The reclustered dataset was then re-annotated according to the enrichment results and manual curation using glial, neuronal, and proliferation markers. Differential Expression was performed using the FindMarkers function in Seurat(v4.0.2)³⁷ with a clustering cut-off of 0.2, having 10 total clusters (0-9) and a differential expression of each cluster against all others and the individual groups (Abx, FMT, and Steady state) against one another.

Neuronal, glial, and cycling signatures were extracted from GO BP pathways and other literature and added as a score using the AddModuleScore function from Seurat. Wishbone (v.0.5.2) was used for trajectory analysis with default settings. All further visualization was executed using ggplot2(v.3.5.1).

Data availability

The raw data files for snRNA-seq and 16S rRNA on SRA and processed single nuclei, 16S, and metabolomics data on GEO are in the process of uploading. They will be available before publication.

Biological material availability

Non-commercially available materials are available upon request.

Statistical analysis

Experiments were performed without investigator blinding. All data points reflect biological replicates on the graphs. The experimental groups included at least three biological replicates. Graphs and statistics were generated using GraphPad Prism v10.3.1. All data are presented as \pm S.E.M. An unpaired two-tailed Student's t-test was used for experiments with two experimental groups. Samples with more than two experimental groups were analyzed using one-way ANOVA and Dunnett's multiple comparison test. Two-way ANOVA with Šidák's multiple comparisons test was used for metabolite concentration (Fig. 2h). Significance levels indicated in the graphs are as follows: * $p < 0.05$, ** $p < 0.01$, *** $p < 0.001$, **** $p < 0.0001$.

References

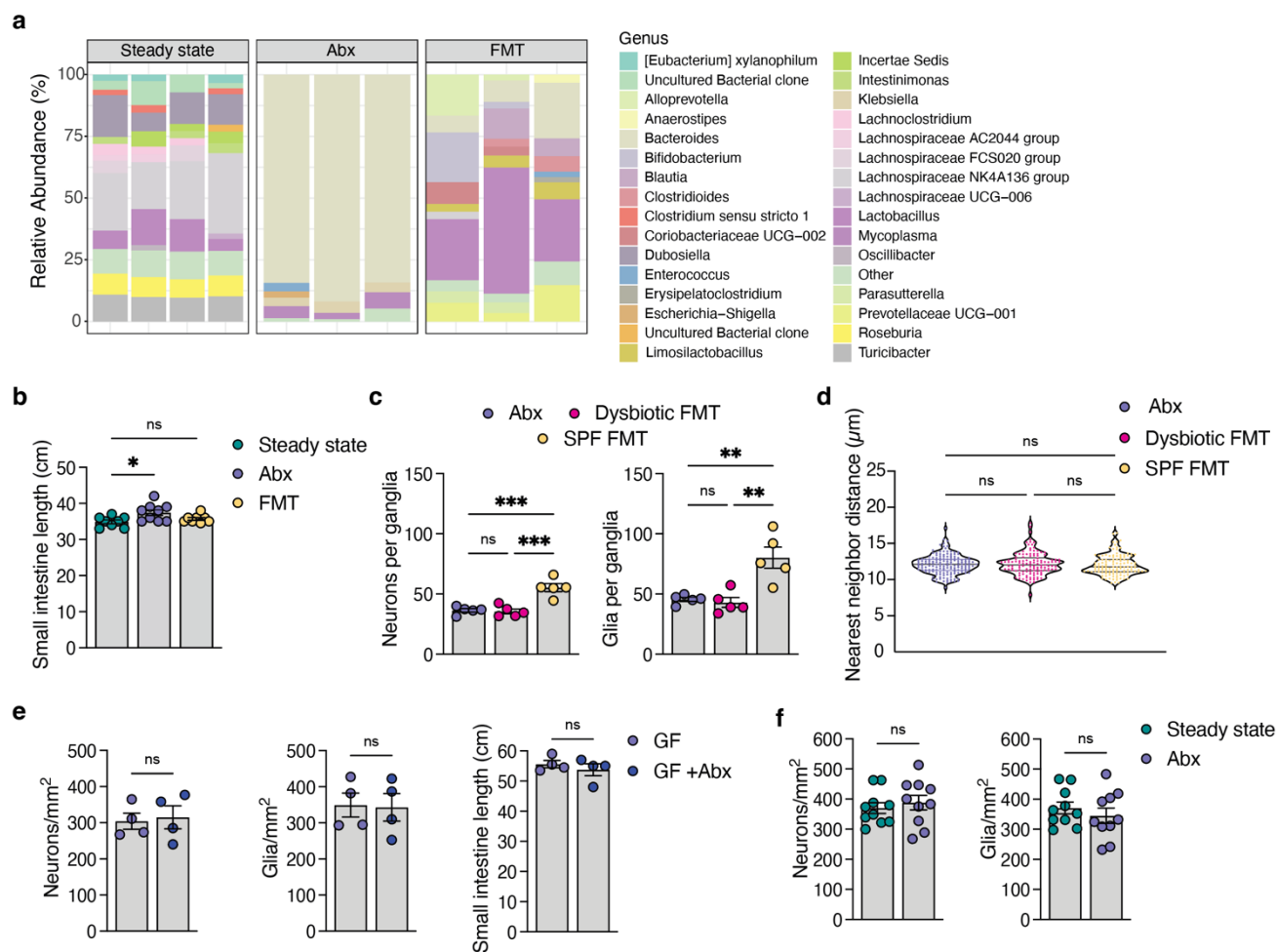
1. Furness, J. B., Rivera, L. R., Cho, H. J., Bravo, D. M. & Callaghan, B. The gut as a sensory organ. *Nat Rev Gastroentero* **10**, 729--740 (2013).
2. Matheis, F. *et al.* Adrenergic Signaling in Muscularis Macrophages Limits Infection-Induced Neuronal Loss. *Cell* **180**, 64--78.e16 (2020).
3. Muller, P. A. *et al.* Microbiota-modulated CART+ enteric neurons autonomously regulate blood glucose. *Science* **370**, 314--321 (2020).
4. White, J. P. *et al.* Intestinal Dysmotility Syndromes following Systemic Infection by Flaviviruses. *Cell* **175**, 1198-1212.e12 (2018).
5. Ahrends, T. *et al.* Enteric pathogens induce tissue tolerance and prevent neuronal loss from subsequent infections. *Cell* (2021) doi:10.1016/j.cell.2021.10.004.
6. Veiga-Fernandes, H. & Mucida, D. Neuro-Immune Interactions at Barrier Surfaces. *Cell* **165**, 801--811 (2016).

7. Mayer, E. A. Gut feelings: the emerging biology of gut–brain communication. *Nat Rev Neurosci* **12**, 453–466 (2011).
8. Sarkar, S. R. & Banerjee, S. Gut microbiota in neurodegenerative disorders. *J Neuroimmunol* **328**, 98–104 (2019).
9. Rao, M. & Gershon, M. D. Enteric nervous system development: what could possibly go wrong? *Nat Rev Neurosci* **19**, 552–565 (2018).
10. Hao, M. M. & Young, H. M. Development of enteric neuron diversity. *J Cell Mol Med* **13**, 1193–1210 (2009).
11. Bergner, A. J. *et al.* Birthdating of myenteric neuron subtypes in the small intestine of the mouse. *J Comp Neurol* **522**, 514–527 (2014).
12. Kabouridis, P. S. *et al.* Microbiota Controls the Homeostasis of Glial Cells in the Gut Lamina Propria. *Neuron* **85**, 289–295 (2015).
13. Joseph, N. M. *et al.* Enteric glia are multipotent in culture but primarily form glia in the adult rodent gut. *J Clin Invest* **121**, 3398–3411 (2011).
14. Belkind-Gerson, J. *et al.* Colitis promotes neuronal differentiation of Sox2+ and PLP1+ enteric cells. *Sci Rep-uk* **7**, 2525 (2017).
15. Laranjeira, C. *et al.* Glial cells in the mouse enteric nervous system can undergo neurogenesis in response to injury. *J Clin Investigation* **121**, 3412–24 (2011).
16. Gabanyi, I. *et al.* Neuro-immune Interactions Drive Tissue Programming in Intestinal Macrophages. *Cell* **164**, 378–391 (2016).
17. Kenneth, N. S. *et al.* An inactivating caspase 11 passenger mutation originating from the 129 murine strain in mice targeted for c-IAP1. *Biochem. J.* **443**, 355–359 (2012).
18. Muller, P. A. *et al.* Microbiota modulate sympathetic neurons via a gut–brain circuit. *Nature* **583**, 441–446 (2020).
19. Brugiroux, S. *et al.* Genome-guided design of a defined mouse microbiota that confers colonization resistance against *Salmonella enterica* serovar Typhimurium. *Nat Microbiol* **2**, 16215 (2016).
20. Vatanen, T. *et al.* Variation in Microbiome LPS Immunogenicity Contributes to Autoimmunity in Humans. *Cell* **165**, 842–853 (2016).
21. Yano, J. M. *et al.* Indigenous Bacteria from the Gut Microbiota Regulate Host Serotonin Biosynthesis. *Cell* **161**, 264–276 (2015).

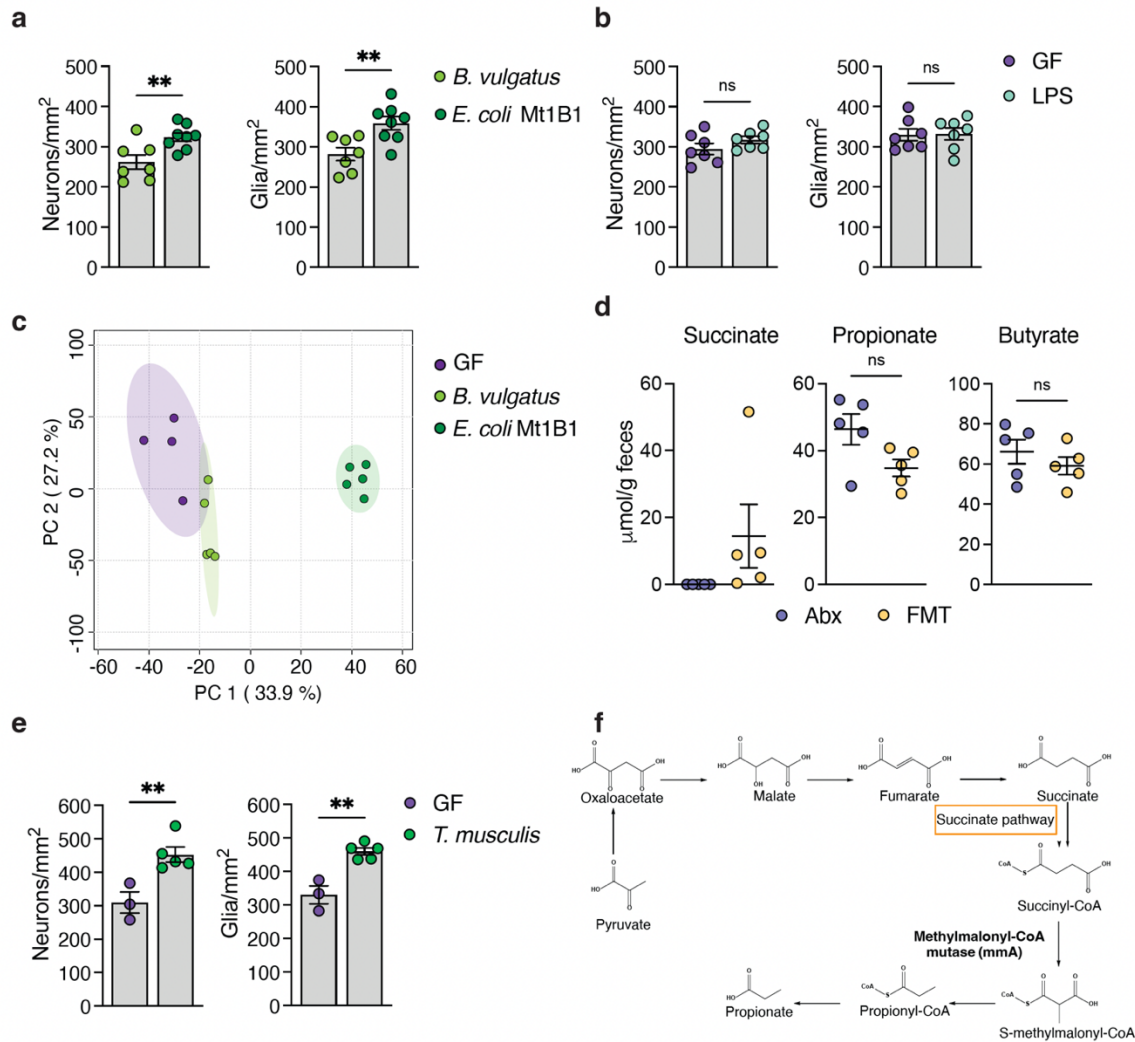
22. Furusawa, Y. *et al.* Commensal microbe-derived butyrate induces the differentiation of colonic regulatory T cells. *Nature* **504**, 446–450 (2013).
23. Erny, D. *et al.* Host microbiota constantly control maturation and function of microglia in the CNS. *Nat Neurosci* **18**, 965–977 (2015).
24. Soret, R. *et al.* Short-Chain Fatty Acids Regulate the Enteric Neurons and Control Gastrointestinal Motility in Rats. *Gastroenterology* **138**, 1772-1782.e4 (2010).
25. Gerrick, E. R. *et al.* Metabolic diversity in commensal protists regulates intestinal immunity and trans-kingdom competition. *Cell* **187**, 62-78.e20 (2024).
26. Wei, Y., Ma, X., Zhao, J., Wang, X. & Gao, C. Succinate metabolism and its regulation of host-microbe interactions. *Gut Microbes* **15**, 2190300 (2023).
27. Nadsombati, M. S. *et al.* Detection of Succinate by Intestinal Tuft Cells Triggers a Type 2 Innate Immune Circuit. *Immunity* **49**, 33-41.e7 (2018).
28. Schneider, C. *et al.* A Metabolite-Triggered Tuft Cell-ILC2 Circuit Drives Small Intestinal Remodeling. *Cell* **174**, 271-284.e14 (2018).
29. Carey, B. W., Finley, L. W. S., Cross, J. R., Allis, C. D. & Thompson, C. B. Intracellular α -ketoglutarate maintains the pluripotency of embryonic stem cells. *Nature* **518**, 413–416 (2015).
30. Baksh, S. C. & Finley, L. W. S. Metabolic Coordination of Cell Fate by α -Ketoglutarate-Dependent Dioxygenases. *Trends Cell Biol.* **31**, 24–36 (2021).
31. Cheng, A. G. *et al.* Design, construction, and in vivo augmentation of a complex gut microbiome. *Cell* **185**, 3617-3636.e19 (2022).
32. Fischbach, M. A. & Sonnenburg, J. L. Eating For Two: How Metabolism Establishes Interspecies Interactions in the Gut. *Cell Host Microbe* **10**, 336–347 (2011).
33. Jin, W.-B. *et al.* Genetic manipulation of gut microbes enables single-gene interrogation in a complex microbiome. *Cell* **185**, 547-562.e22 (2022).
34. Laranjeira, C. *et al.* Glial cells in the mouse enteric nervous system can undergo neurogenesis in response to injury. *The Journal of Clinical Investigation* **121**, (2011).
35. Kulkarni, S. *et al.* Adult enteric nervous system in health is maintained by a dynamic balance between neuronal apoptosis and neurogenesis. *Proc National Acad Sci* **114**, E3709–E3718 (2017).
36. Kuleshov, M. V. *et al.* Enrichr: a comprehensive gene set enrichment analysis web server 2016 update. *Nucleic Acids Res.* **44**, W90–W97 (2016).

37. Butler, A., Hoffman, P., Smibert, P., Papalexi, E. & Satija, R. Integrating single-cell transcriptomic data across different conditions, technologies, and species. *Nat. Biotechnol.* **36**, 411–420 (2018).
38. Pook, C., Ahrens, J. M. & Clagett-Dame, M. Expression pattern of Nav2 in the murine CNS with development. *Gene Expr. Patterns* **35**, 119099 (2020).
39. Setty, M. *et al.* Wishbone identifies bifurcating developmental trajectories from single-cell data. *Nat Biotechnol* **34**, 637–645 (2016).
40. Mo, A. *et al.* Epigenomic Signatures of Neuronal Diversity in the Mammalian Brain. *Neuron* **86**, 1369--1384 (2015).
41. Guyer, R. A. *et al.* Single-Cell Multiome Sequencing Clarifies Enteric Glial Cell Diversity and Identifies an Intraganglionic Population Poised for Neurogenesis. *Biorxiv* 2021.08.24.457368 (2022)
doi:10.1101/2021.08.24.457368.
42. Scavuzzo, M. A. *et al.* Enteric glial hub cells coordinate intestinal motility. *bioRxiv* 2023.06.07.544052 (2023)
doi:10.1101/2023.06.07.544052.
43. Guyer, R. A. *et al.* Single-cell multiome sequencing clarifies enteric glial diversity and identifies an intraganglionic population poised for neurogenesis. *Cell Reports* **42**, 112194 (2023).
44. Rao, M. *et al.* Enteric glia express proteolipid protein 1 and are a transcriptionally unique population of glia in the mammalian nervous system. *Glia* **63**, 2040–2057 (2015).
45. Reddien, P. W. The purpose and ubiquity of turnover. *Cell* **187**, 2657–2681 (2024).
46. McCallum, S. *et al.* Enteric glia as a source of neural progenitors in adult zebrafish. *Elife* **9**, e56086 (2020).
47. Goncalves, J. T., Schafer, S. T. & Gage, F. H. Adult Neurogenesis in the Hippocampus: From Stem Cells to Behavior. *Cell* **167**, 897--914 (2016).
48. Lim, D. A. & Alvarez-Buylla, A. The Adult Ventricular–Subventricular Zone (V–SVZ) and Olfactory Bulb (OB) Neurogenesis. *Cold Spring Harb. Perspect. Biol.* **8**, a018820 (2016).
49. Laddach, A. *et al.* A branching model of lineage differentiation underpinning the neurogenic potential of enteric glia. *Nat. Commun.* **14**, 5904 (2023).
50. Jopling, C., Boue, S. & Belmonte, J. C. I. Dedifferentiation, transdifferentiation and reprogramming: three routes to regeneration. *Nat Rev Mol Cell Bio* **12**, 79–89 (2011).
51. Arai, Y. *et al.* Neural stem and progenitor cells shorten S-phase on commitment to neuron production. *Nat. Commun.* **2**, 154 (2011).

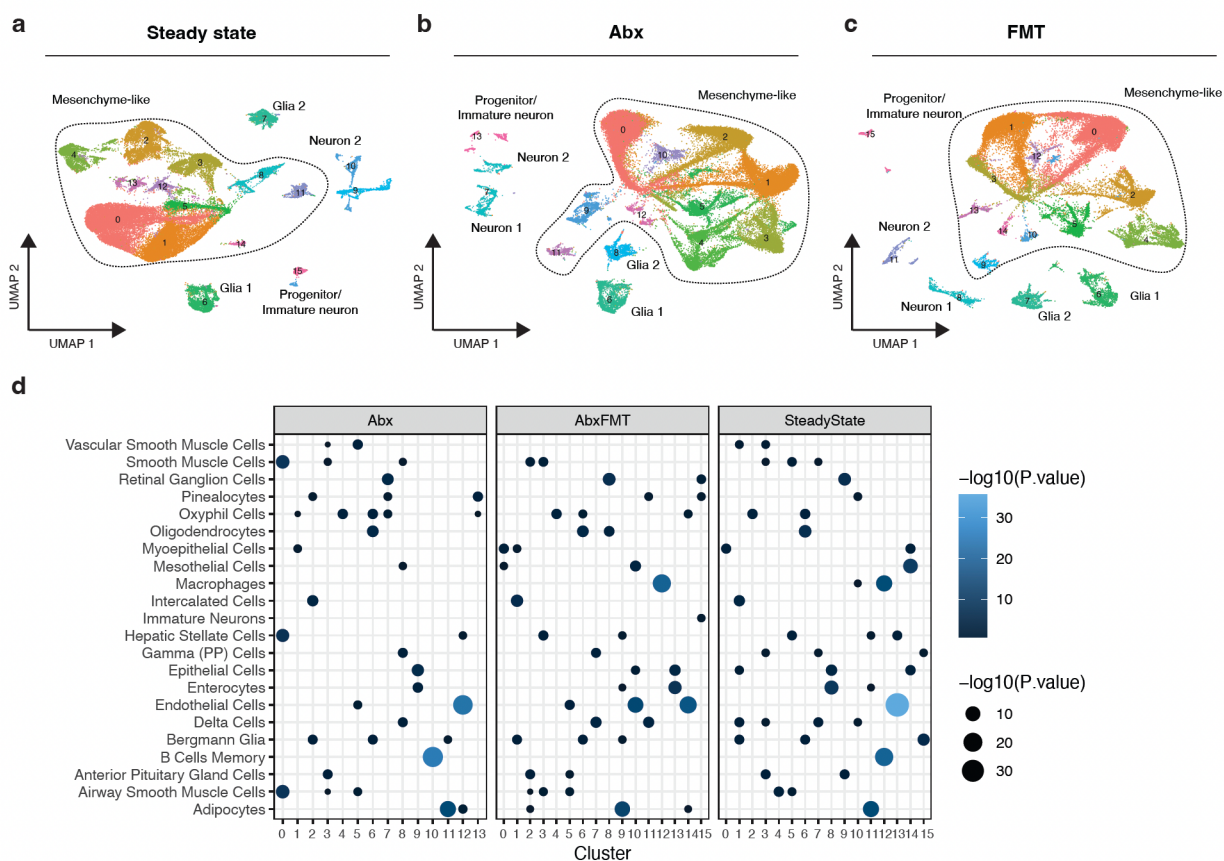
52. Ganier, O. *et al.* Mitosis without DNA replication in mammalian somatic cells. *bioRxiv* 2020.07.08.193607 (2020) doi:10.1101/2020.07.08.193607.
53. He, W. *et al.* Citric acid cycle intermediates as ligands for orphan G-protein-coupled receptors. *Nature* **429**, 188–193 (2004).
54. Reddy, A. *et al.* pH-Gated Succinate Secretion Regulates Muscle Remodeling in Response to Exercise. *Cell* **183**, 62–75.e17 (2020).
55. Ahrends, T., Weiner, M. & Mucida, D. Isolation of myenteric and submucosal plexus from mouse gastrointestinal tract and subsequent flow cytometry and immunofluorescence. *STAR Protoc.* **3**, 101157 (2022).
56. Caporaso, J. G. *et al.* Global patterns of 16S rRNA diversity at a depth of millions of sequences per sample. *Proc. Natl. Acad. Sci.* **108**, 4516–4522 (2011).
57. McMurdie, P. J. & Holmes, S. phyloseq: An R Package for Reproducible Interactive Analysis and Graphics of Microbiome Census Data. *PLoS ONE* **8**, e61217 (2013).
58. Pang, Z. *et al.* MetaboAnalystR 4.0: a unified LC-MS workflow for global metabolomics. *Nat. Commun.* **15**, 3675 (2024).
59. Schindelin, J. *et al.* Fiji: an open-source platform for biological-image analysis. *Nat. Methods* **9**, 676–682 (2012).
60. Stringer, C., Wang, T., Michaelos, M. & Pachitariu, M. Cellpose: a generalist algorithm for cellular segmentation. *Nat Methods* **18**, 100–106 (2021).
61. Xu, S. *et al.* Using clusterProfiler to characterize multiomics data. *Nat. Protoc.* 1–29 (2024) doi:10.1038/s41596-024-01020-z.
62. Korotkevich, G. *et al.* Fast gene set enrichment analysis. *bioRxiv* 060012 (2021) doi:10.1101/060012.



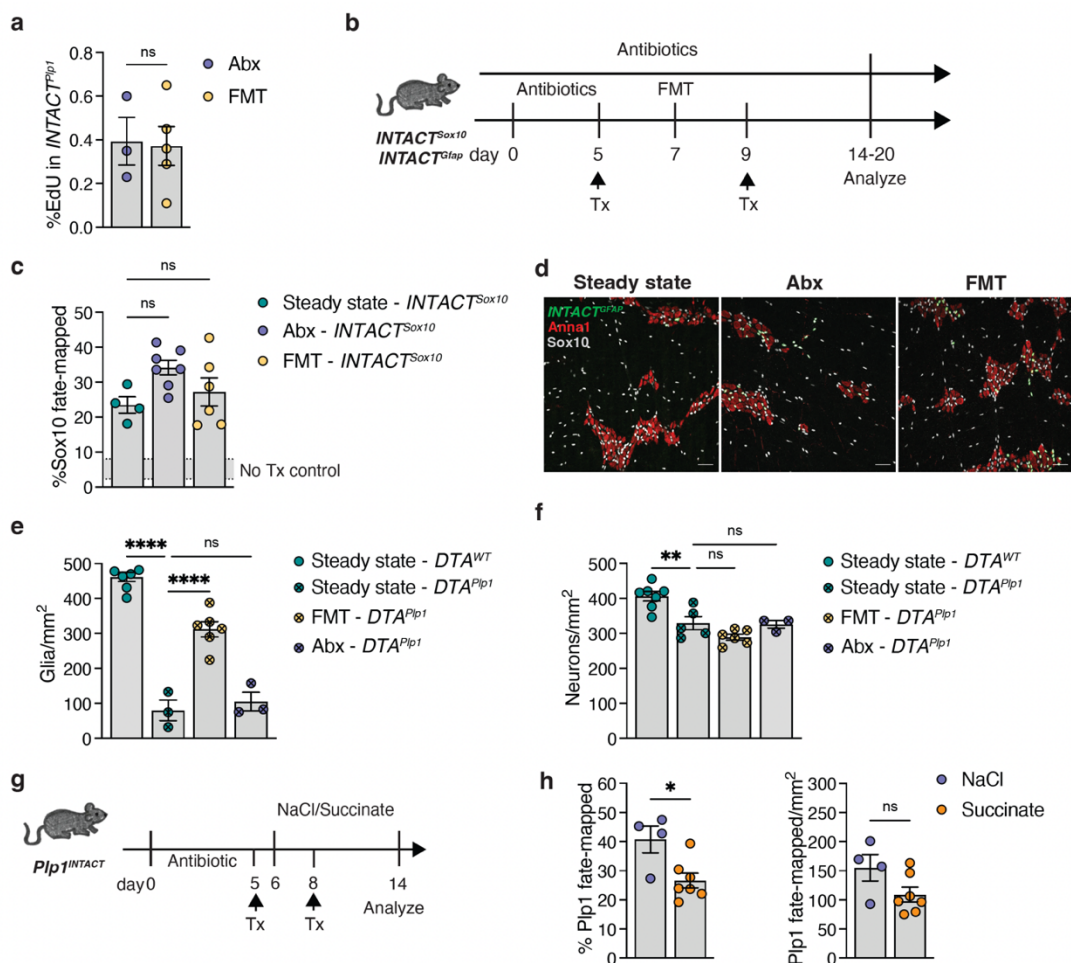
Extended Data Fig. 1: The effects of antibiotics and fecal microbiota transfer on ENS. (a) The percent relative abundance of gut microbes at the genus level was analyzed by 16S RNA sequences from fecal samples (n=4 steady state, n=3 Abx, n=3 FMT). (b) Small intestine length of mice harvested at the endpoint (n=8 steady state, n=9 Abx, n=8 FMT). Data are representative of at least two experiments. (c) Average number of neurons (left) and Sox10+ glia (right) per ganglia across different conditions (n=5). The same samples were analyzed, as shown in Fig. 1g. (d) Distance between cells within the ganglia is represented as the nearest neighbor distance (n=5). The same samples were analyzed, as shown in Fig. 1g. (e) Swiss Webster germ-free mice treated with antibiotics in drinking water for seven days. Quantification of neurons (left) and intraganglionic glia (middle) per mm^2 area is shown, along with the total changes in small intestine length (right) (n=4). (f) Quantification of neurons (left) and intraganglionic glia (right) per mm^2 area in steady-state or antibiotic-treated 129S1/SvImJ mice deficient in Caspase 11. All data are mean \pm S.E.M. One-way ANOVA with multiple hypothesis testing was used for b, c, and d. Unpaired two-tailed Student's t-test was used for e and f.



Extended Data Fig. 2: Characterization of the impact of succinate on ENS regeneration. (a) Quantification of neurons (left) and intraganglionic glia (right) per mm² area in germ-free (GF) Swiss Webster mice monocolonized with *B. vulgatus* and *E. coli* Mt1B1 for 7-10 days (n=7 *B. vulgatus*, n=8 *E. coli* Mt1B1). Data are representative of at least two independent experiments. (b) Quantification of neurons (left) and intraganglionic glia (right) per mm² area in GF Swiss Webster mice treated with oral gavage of LPS derived from *E. coli* for five days (n=7). The mice were analyzed on day 7. Data are representative of at least two independent experiments. (c) PCA analysis of untargeted cecal metabolomics data of C57BL/6 GF monocolonized with *B. vulgatus* and *E. coli* Mt1B1 for seven days (n=5). (d) HPLC-MS quantification of Succinate and Propionate levels in C57BL/6 mice treated with Abx or received FMT from SPF mice (n=5). The mice were analyzed seven days post-FMT. (e) Quantification of neurons (left) and intraganglionic glia (right) per mm² area in GF C57BL/6 mice monocolonized with the protist *T. musculus* for seven days (n=3 GF, n=5 *T. musculus*). (f) Schematic representation of the carbohydrate catabolic pathway in Bacteroides. All data are mean ± S.E.M. Unpaired two-tailed Student's t-tests were used for a, b, d, and e. All data are from the ileum myenteric plexus.



Extended Data Fig. 3: snRNA-seq characterization of the whole-tissue ileum muscularis layer. UMAP clustering of snRNA-seq datasets of the whole tissue ileum muscularis layer at steady state (a), Abx (b), and FMT (c). (d) Dot plot showing the p-values for GSEA enrichment of the top 10 pathways enriched in all clusters and filtered by a list of all the most enriched pathways per cluster. These pathways and a curated gene list were used to manually annotate clusters a, b, and c.



Extended Data Fig. 4: Alternative mechanisms of neuronal regeneration in injury and recovery states.

(a) The percentage of EdU+ *INTACT*^{Plp1} labeled glia in Abx and FMT assessed by flow cytometry 3 days post-FMT (n=3 Abx, n= 4 FMT). (b) Schematic representation of the experimental design of the *INTACT*^{Sox10} and *INTACT*^{GFAP} glia fate-mapping experiments. (c) Quantification of the percentage of *INTACT*^{Sox10}+Anna1+ cells over total Anna1+ cells (left) and number of *INTACT*^{Sox10}+Anna1+ cells per mm² of ileum myenteric plexus 7-10 days post-Abx or FMT (n=4 steady state, n=7 Abx, n=6 FMT). Steady-state mice were treated with tamoxifen and analyzed 24h later. The grey shaded line indicates the distribution of the baseline labeling in the No Tamoxifen control. Data are representative of at least two independent experiments. (d) Confocal microscopy images of ileum myenteric plexus of *INTACT*^{GFAP} (green) reporter mice immunostained for ANNA1 and Sox10. Scale bars, 50 μm. We did not observe *INTACT*^{GFAP}+Anna1+ double positives in at least two independent experiments, with n > 5 mice per group. (e) Quantification of intraganglionic glia (Sox10) in ileum myenteric plexus of *DTA*^{WT} or *DTA*^{Plp1} Plp1+ glia ablated mice (steady-state *DTA*^{WT} and FMT *DTA*^{Plp1}, n=6. Steady-state *DTA*^{Plp1} and Abx *DTA*^{Plp1}, n=3). *DTA*^{WT} and *DTA*^{Plp1} FMT are the same data from Fig. 4e. (f) Quantification of neurons in ileum myenteric plexus of *DTA*^{WT} or *DTA*^{Plp1} Plp1+ glia ablated mice (steady-state *DTA*^{WT} n=7, FMT *DTA*^{Plp1} n=5, steady-state *DTA*^{Plp1} n=5, Abx *DTA*^{Plp1}, n=3). (g) Schematic representation of the experimental design of *INTACT*^{Plp1} glia fate-mapping experiment in succinate recovery model after Abx treatment (h) Quantification of the percentage of *INTACT*^{Plp1}+Anna1+ cells over total Anna1+ cells (left) and number of *INTACT*^{Plp1}+Anna1+ cells per mm² of ileum myenteric plexus seven days post-Abx or FMT (n=4 NaCl, n=7 Succinate). Data are representative of at least two independent experiments. All data are mean ±S.E.M. An

unpaired two-tailed Student's t-test was used for **a**, **h**, and one-way ANOVA with multiple hypothesis testing was used for **c**, **e**, and **f**. All data are from the ileum myenteric plexus.